



**HAL**  
open science

# Homogenization Based Topology Optimization of a Coupled Thermal Fluid-Structure Problem

Godfred Oheneba Agyekum, Laurent Cangémi, François Jouve

► **To cite this version:**

Godfred Oheneba Agyekum, Laurent Cangémi, François Jouve. Homogenization Based Topology Optimization of a Coupled Thermal Fluid-Structure Problem. 2023. hal-04108556v1

**HAL Id: hal-04108556**

**<https://hal.science/hal-04108556v1>**

Preprint submitted on 27 May 2023 (v1), last revised 1 Sep 2023 (v2)

**HAL** is a multi-disciplinary open access archive for the deposit and dissemination of scientific research documents, whether they are published or not. The documents may come from teaching and research institutions in France or abroad, or from public or private research centers.

L'archive ouverte pluridisciplinaire **HAL**, est destinée au dépôt et à la diffusion de documents scientifiques de niveau recherche, publiés ou non, émanant des établissements d'enseignement et de recherche français ou étrangers, des laboratoires publics ou privés.



Distributed under a Creative Commons Attribution 4.0 International License

# Homogenization Based Topology Optimization of a Coupled Thermal Fluid-Structure Problem

Godfred Oheneba Agyekum<sup>1\*</sup>, Laurent Cangémi<sup>1†</sup>  
and François Jouve<sup>2†</sup>

<sup>1\*</sup>IFP Energies nouvelles, Rueil-Malmaison, 92852, France.

<sup>2</sup>Université Paris Cité, Laboratoire Jacques-Louis Lions (LJLL),  
Paris, F-75006, France.

\*Corresponding author(s). E-mail(s):

[godfred.a.o.ezail@gmail.com](mailto:godfred.a.o.ezail@gmail.com);

Contributing authors: [laurent.cangemi@ifpen.fr](mailto:laurent.cangemi@ifpen.fr);

[francois.jouve@u-paris.fr](mailto:francois.jouve@u-paris.fr) ;

†These authors contributed equally to this work.

## Abstract

Homogenization method is applied to topology optimization of a weakly coupled three physics problem, where structures are made of periodically perforated material. The microscopic periodic cell is macroscopically modulated, where the design is characterized by the material density and its homogenized Hooke's law at each point of the domain. The coupling is weak because the three physics involved are solved consecutively: first, the coupled fluid flow is determined using Biot-Darcy's law, second, the thermal model using the convection-diffusion equation and third, the three-physic problem by solving the linear poro-thermo elasticity system; our aim is to optimize the homogenized formulation of this system. This approach permits a computationally low cost of evaluation of load sensitivities using the adjoint-state method. Numerical two-dimensional and moderately large-scale three-dimensional two or three-physic problems are presented using the alternate directions algorithm. It is demonstrated how the implementation can address a variety of design problems.

**Keywords:** Topology optimization, multi-scale, periodic homogenization, porous medium, adjoint methods, fluid-structure interaction, convective heat-transfer

# 1 Introduction

The ambition to develop simulation methods making it possible to predict the integrity or properties of use (mechanical, diffusive, thermal, electromagnetic, vibratory, etc.) of structures (industrial or natural), materials or processes involved in the development of new advanced technologies is growing consistently. Herein, homogenization-based method is proposed to investigate shape optimization problems for a weakly coupled model of heat propagation, fluid flow and structure strain and, making it possible to consider a weak coupling between the three physics at stake because one can assume that the fluid domain is fixed at first order. However, we should bear in mind that this weak coupling is a major simplification and therefore reduces the computational cost.

A comprehensive overview of shape optimization with the homogenization method is provided by [1] and, for a general summary of the homogenization method, we refer the reader to [2–7] and references therein. It is worth to note that, this approach provides a consistent way for computing effective material with microstructures (composite materials) and that, once the optimal composite is obtained by homogenization-based topology optimization method, we might need to dehomogenize the solution: see [8], for periodically perforated materials. The design method described in this paper is strongly inspired by the works mentioned above as well as being related to modern production techniques such as additive manufacturing.

A typical shape optimization problem arising in this context involves an objective function, depending on the geometries of the fluid and solid subdomains and, where the whole domain is described by a density function (material density) that can take on values in the interval  $[0, 1]$ , which has to be minimized under some constraints (e.g., volume or mass constraints). This allows to compute the sensitivities with respect to design variables using the adjoint-state method [1, 9, 10], introducing adjoint states. For these adjoint states, which are to be solved, it turns out that the coupling is reversed for the adjoint system: the elasticity is solved first, followed by the convection-diffusion equation and the fluid model.

Shape optimization that involve pressure-loaded or thermal fluid-loaded boundaries has been conducted also by [11–23]. In [11–15], the authors deduce the topology or layout based on boundary motion and, using in [11, 12, 15], the iso-density method to identify the pressure loading facets: Bézier spline curves were used to describe the pressure-loaded facets. This allows in [11, 12], to evaluate the sensitivities with respect to design variables using the finite difference formulation and, in [15], to provide an analytical method to calculate load sensitivities. Note that in [11, 12, 15], the considered sensitivities were restricted to only the pressure-loaded boundaries.

In contrast, the works in [13, 14, 16] do not account for load sensitivities within their topology optimization setting: in [13], the pressure-loaded facets is predefined and, an additional set of variables is used, which are optimized along with the design variables; whereas in [14], an element-based search method

is employed to identify the pressure-loaded facets and in [16], an algorithm based on digital image processing and regional contour tracking is proposed to generate the pressure loading surface.

On the other hand, in [17], the authors deduce the topology optimization based on binary structures method to design structures that consider buckling constraints and loaded by design-dependent fluid pressure loads: it adopts binary design variables and handles multiple constraints solved by an integer linear programming scheme, where sensitivity filtering method is proposed.

In contrast to methods using boundary motion, in [18–20], the authors deduce the topology based on level-set methods: an implicit boundary description is available and, using to identify the pressure load. In [18], the Distance Regularized Level Set Evolution is proposed to capture the structural boundary and, using the zero level contour of a level-set function to represent the loaded-pressure boundary but did not account load sensitivities; whereas in [19], the Laplace’s equation approach is employed to compute hydrostatic fluid pressure fields and, also, a flood fill procedure to capture the solid/fluid interface: shape sensitivities in conjunction with Ersatz material interpolation method are used within their approach. Recently in [20], Hadamard’s method of shape differentiation is applied to shape and topology optimization of a coupled thermal fluid-structure problem in a level set mesh evolution framework: sensitivity analysis is performed with respect to the geometry of the interface between the fluid and solid domain, using the Hadamard’s method of shape differentiation, introducing adjoint states.

Moreover, unlike boundary motion or level-set methods, in [21, 22], the authors deduce the topology using density-based approach: shape optimization problems are transformed to material distribution problems using fictitious composite materials and, without identifying loading surfaces directly. In [21], a density-based topology optimization is proposed to design both structures and compliant mechanisms loaded by design-dependent pressure loads: Darcy’s law in conjunction with a drainage term is proposed to treat the pressure loads, which are transferred into a design dependent pressure field using a partial differential equation, which is solved using the finite element method; the load sensitivities are computed using the adjoint-variable method. Recently in [22](2023), is developed per the approach first reported in [21], a MATLAB implementation TOPress, using the method of moving asymptotes.

In contrast, the density-based method presented in [23] is based on true composite materials: two material constituents, substance and void, are considered, and the microscopic optimal void distribution is considered. An important feature of the procedure is that the homogenization method is applied to determine macroscopic constitutive equations for the material with microscopic material constituents. In [23], the porous material is described as the Biot continuum derived by the homogenization of two decoupled problems: deformation of a porous solid saturated by a slightly compressible static fluid, first and, Stokes flow through the rigid porous structure, second. The effective medium (composite) properties are given by the drained skeleton elasticity, the

Biot stress coupling, the Biot compressibility coefficients, and by the hydraulic permeability of the Darcy flow model: these are computed using characteristic responses of the representative unit cell constituted by an elastic skeleton (solid) and by the fluid channel (void); the adjoint-state method is proposed to evaluate sensitivities of objective functions constituted by the Biot model coefficients with respect to the underlying pore shape described by a B-spline box which embeds the whole representative cell and, where the gradient-based method is employed to solve the optimization problems: the shape derivatives of the homogenized coefficients are derived using the shape sensitivity technique and the material derivative approach.

In this article, we present a new approach to design structures subjected to thermal loads and cooled down by a fluid-pressure and, this falls within the general framework of density methods where phenomenological laws of equivalent media is derived by the homogenization method. In this regard, the presented approach falls within the framework of recent work in [21, 23] where Darcy’s flow model is used to describe the fluid flow. However, the approach in [21] is different since the continuous problem does not contain a model that explicitly couples the fluid pressure to the solid skeleton and thus, it induces difficulties in the modeling where a volumetric force is added intuitively in the elastic problem without it being explicitly defined as the result of a continuous physical law. Moreover, compared to [23], the porous material is described as the Biot-Darcy continuum derived by the homogenization of a weakly coupled three physics problem: deformation of a porous-thermoelastic saturated by incompressible fluid pressure (satisfying Biot-Darcy’s law), first, the convection-diffusion equation for the temperature, second and, cool down by a Biot-Darcy’s flow through the rigid porous thermoelastic, third. The effective medium properties are given by the undrained skeleton elasticity, the Biot stress coupling, the Biot coefficient, the thermal coefficients and conductivity for the convection-diffusion model and, by hydraulic permeability of the Darcy flow model: these are computed using characteristic responses of the representative unit cell, namely, a perforated hexagonal cell in 2-D or the tetrakaidecahedron cell in 3-D, constituted by a solid phase and void; see Fig. 1 and Fig. 3. Hence, the fluid pressure can be seen as a pore pressure acting on the solid part of the ”equivalent porous thermoelastic” through a Biot coefficient, which is density-dependent and, where the physical laws derived from the mechanics of porous media make it possible to link this coefficient to the local (matrix) and global (porous medium) moduli of compressibility of the solid system. This allows to provide sensitivities of general ”smooth enough” objection functions with respect to design variables using the adjoint-state method, introducing adjoint-states; the homogenized coefficients are derived using the Lagrangian method and the projected gradient algorithm: in [23], the shape sensitivity technique and the material derivative approach are employed. Of course, these shape derivatives are at the basis of our gradient-based alternate directions algorithm [1], which is used for our numerical simulations. In summary, we present the following aspects:

- homogenized Biot-Darcy’s law is used to characterize the fluid flow through a true composite material,
- the convection–diffusion equation is used for the temperature,
- we weakly couple the fluid loads to the linearized thermoelasticity system for the solid displacement,
- the approach facilitates computationally inexpensive evaluation of the load sensitivities with respect to design variables using the adjoint-state method, introducing adjoint-states,
- the flow coefficient, Biot’s coefficient and conductivity coefficients are derived using the homogenization method,
- the approach avoids explicit description of the loading boundary,
- the robustness and efficiency of the approach is demonstrated through several design problems, using the alternate directions algorithm.

The remainder of this paper is structured as follows: in Section 2, we briefly recall the necessary ingredients of the homogenization method and we explain our strategy. First, choose a parametrized periodicity cell. Second, we compute its effective properties for the entire range of its parameters. In Section 3, we give a precise account of our weakly coupled model of heat propagation, fluid flow and structure strain. In Section 4, first, we introduce the optimization problem formulation, which turns out to be a simple parametric optimization problem since our periodicity cell is parametrized. Section 5, is concerned with our topology optimization algorithm: it is an alternate directions algorithm, which successively computes the stress field through the solving of a weakly coupled three physics problem. Finally, our numerical results are presented in Section 6: 2-D and 3-D computations are displayed of various design problems involving two or three-physic for arbitrary objective functions; and we summarize our findings and give an outlook in Section 7.

## 2 Periodic homogenization

The mathematical framework of the homogenization theory can be found in [1]. In this section, we briefly present the principles of this method and explain our strategy. We restrict our analysis to locally periodic hexagonal cell in 2-D and tetrakaidecahedron cell in 3-D. Note that, it should be possible to adapt the whole method (or at least part of it) to periodic square cells (in 2-D) or to other similar geometry as the tetrakaidecahedron cells (in 3-D). Our aim is to determine the homogenized physical properties of such materials when varying their parameter; it is a preprocessing stage, which can be performed off-line. It is independent of the objective function, computational domain, applied loads or boundary conditions. The Hooke’s laws are computed by solving the so-called cell problems, that describe the deformation at the scale of the microstructure, which is a very classical task in homogenization theory.

## 2.1 Set of admissible microstructures

From now on, we restrain our analysis to a simple class of composites already introduced in [28], repeated periodically on the whole space.

### 2.1.1 Smooth honeycomb cell.

Let  $Y$  be the periodic smooth honeycomb cell: similar to the classical honeycomb cell (i.e., an hexagonal cell with perforated hexagonal central hole), except that the interior corners of the perforated hexagonal hole are rounded; see Fig. 1 and Fig. 2. As a consequence, if the density  $\theta$  in  $[0, 1]$ , tends to 1, the central smooth hexagon tends to a circle with a diameter going to 0. However, because of its rounded corners, the smooth honeycomb can not reach complete void:  $\theta$  going to zero is excluded. In this context, for practical reason, the smooth honeycomb is (contrary to the classical one, which is parametrized by the density) parametrized by another parameter  $h \in [0, 1]$ , homogeneous to a distance. Indeed, in order to design this kind of cell, a parametric curve  $\Gamma_h$  (which depends on  $h$ ) is introduced and represents the boundary of the perforated smooth central hole.

We now introduce some notations before giving its polar equation. Let  $v(t) = (\cos(t), \sin(t))^T$  and  $n_i$  (for  $i \in \{0, 1, 2\}$ ) represent the normal vectors of the three diagonals of  $Y(h)$ , that are:

$$n_0 = \begin{pmatrix} 0 \\ 1 \end{pmatrix}, \quad n_1 = \begin{pmatrix} \frac{\sqrt{3}}{2} \\ \frac{1}{2} \end{pmatrix}, \quad n_2 = \begin{pmatrix} \frac{\sqrt{3}}{2} \\ -\frac{1}{2} \end{pmatrix}. \quad (1)$$

The polar equation of the parametric curve  $\Gamma_h$  (of smooth hexagon hole) is defined by:

$$r(t) = h \frac{\sqrt{3}}{2} \left( \sum_{i=0}^2 |v(t) \cdot n_i|^{k(h)} \right)^{\frac{-1}{k(h)}} \quad \text{with } t \in [0, 2\pi], \quad (2)$$

where  $k$  is positive coefficient, which depends on  $h$ : for this work, we took  $k(h) = 4 + 20h^2$ . Note that  $h$  is homogeneous to a distance, similar to the parameter

$$m = \frac{\sqrt{3}}{2} (1 - \sqrt{1 - \theta}),$$

which denotes the relative width of bars with respect to the size of the periodic cell  $Y(h)$ ; see Fig. 1(b). In the following, we give some remarks over the polar equation of the parametric curve  $\Gamma_h$ , which can be extended to other polygons. Let  $\mathcal{H}$  be a regular unit hexagon, namely, the set of all points such that the maximal distance of a point in  $\mathcal{H}$  from the three diagonals is equal to  $\frac{\sqrt{3}}{2}$  and, let  $M(r, t)$  be a point, with its polar coordinate denoted  $(r, t)$ . Thus,  $M$  is a

point in  $\mathcal{H}$  if and only if, its polar coordinate  $(r, t)$  satisfies

$$r \max_i |v(t) \cdot n_i| = \frac{\sqrt{3}}{2}. \quad (3)$$

Hence, the polar equation of  $\mathcal{H}$  verifies

$$r(t) = \frac{\sqrt{3}}{2} (\max_i |v(t) \cdot n_i|)^{-1}. \quad (4)$$

And, as a consequence, we get that

$$\left( \sum_{i=0}^2 |v(t) \cdot n_i|^k \right)^{-\frac{1}{k}} \rightarrow_{k \rightarrow \infty} \max_i |v(t) \cdot n_i|. \quad (5)$$

Note that, the polar equation of  $\Gamma_h$  comes from combining the polar equation of  $\mathcal{H}$  and the above limit; the parameter  $h$  is added in order to adjust the diameter of its inner hole. Here, our interest for the smooth honeycomb relies on its smooth rounded corners, known to generate lower local concentration stress ([29, 30]), compared to the classical honeycomb.

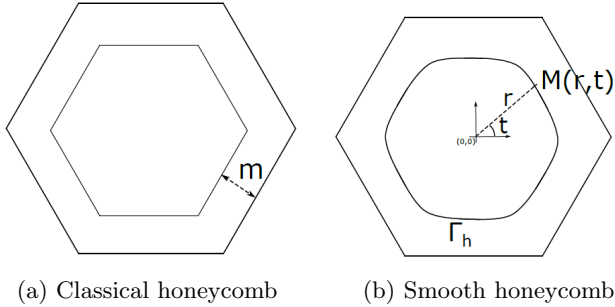


**Fig. 1** Isotropic design cells (images taken from [28])

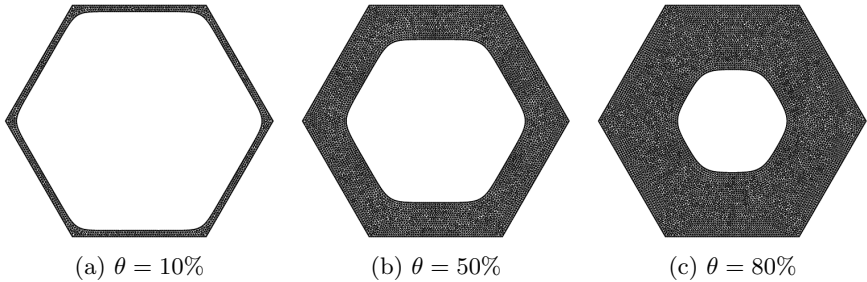


**Fig. 2** The Smooth honeycomb cell for different values to the density  $\theta$



### 2.1.2 Tetrakaidecahedron cell.

In 3-D, isotropic cells are not so easy to design. Here, we design a regular tetrakaidecahedron, known as the Kelvin foam, similar to the one introduced in [28, 32] and, it is shown to yield isotropic (or quasi isotropic) homogenized Hooke's laws. Its features fourteen faces: six unit squares and eight regular unit hexagons; see Fig 3 and Fig 4. Several approaches are possible in order to design isotropic cells from this one, parametrized by one parameter, the local density. A naive approach consists in adding a central tetrakaidecahedron inclusion characterized by the size in  $[0, 1]$ .

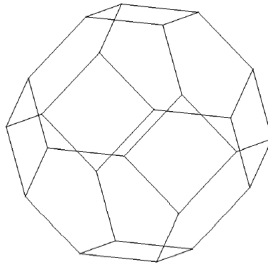


**Fig. 3** Tetrakaidecahedron: an isotropic design cell in 3-D (image taken from [28]).

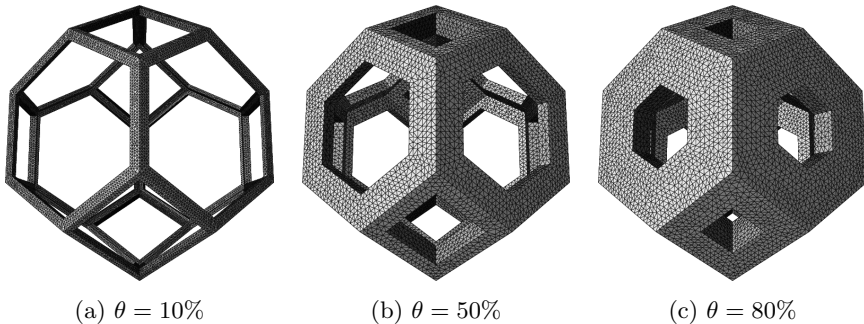


**Fig. 4** Tetrakaidecahedron (i.e., Kelvin foam) for different values of the material density  $\theta$ .

## 2.2 Cell problem and homogenized elasticity tensor

Here, we only give a few important results on the theory of homogenization; the interested reader will find more details in [1].

Assume that, in a given macroscopic domain  $\Omega$ , there is a periodic distribution of holes inside an isotropic elastic material, with constant elastic tensor  $A$ . Let  $\epsilon > 0$  be the periodic size and, let  $Y$  be the periodic pattern: either the regular

smooth hexagon in 2-D or the regular tetrakaidecahedron in 3-D. The periodicity of  $Y$  is defined by the same displacement on two opposite and parallel faces; hence for the hexagonal cell in 2-D, there are three directions of periodicity and for the tetrakaidecahedron cell in 3-D, there are seven directions of periodicity; see Fig. 1 and Fig. 3. Let  $Y_0$  be the solid part in  $Y$  and, we denote by  $|Y|$ , the volume of the periodic cell  $Y$ ; let  $\Gamma$  be the boundary of the holes (i.e., the interface solid/void) and  $\mathbf{n}$  be the normal vector to the boundary  $\Gamma$ . In addition, assume that whenever  $\epsilon$  tends to zero, the porous medium can be considered homogeneous, with effective tensor denoted  $A^*(x)$ . To compute the homogenized tensor  $A^*$ , one needs the so-called correctors  $w_{ij}$ , corresponding to the local displacements in the periodic cell  $Y$ , defined for each pair  $(i, j) \in \{1, \dots, N\}$  ( $N \in \{2, 3\}$ ) as the solutions to the following set of equations:

$$\begin{cases} \operatorname{div}(A(e_{ij} + e(w_{ij}))) = 0 & \text{in } Y \\ A(e_{ij} + e(w_{ij})) \cdot \mathbf{n} = 0 & \text{on } \Gamma \\ y \mapsto w_{ij}(y) & Y\text{-periodic,} \end{cases} \quad (6)$$

where  $e_{ij} = \frac{1}{2}(e_i \otimes e_j + e_j \otimes e_i)$  represents the basis of the symmetric tensors of order 2. As a consequence, the variational formulation associated to (6) is defined, that is: find  $w_{ij} \in H_{\#}^1(Y, \mathbb{R}^N) = \{w \in H^1(Y, \mathbb{R}^N) \mid w \text{ is } Y\text{-periodic}\}$  such that

$$\forall \phi \in H_{\#}^1(Y, \mathbb{R}^N) \quad \int_Y A e(w_{ij}) : e(\phi) + \int_Y A e_{ij} : e(\phi) = 0, \quad (7)$$

which admits a unique solution (up to a rigid displacement field). The entries of  $A^*(x)$  are then defined in terms of the correctors  $w_{ij}$  (solutions of (6)), that are:

$$A_{ijkl}^* = \frac{1}{|Y|} \int_Y A(e_{ij} + e(w_{ij})) : (e_{kl} + e(w_{kl})) \, dy \quad \forall i, j, k, l \in \{1, \dots, N\} \quad (8)$$

We emphasize that, to compute the homogenized tensor  $A^*$ , only three of its coefficients are needed (e.g.,  $A_{1111}^*$ ,  $A_{1122}^*$  and  $A_{1212}^*$ ) to fully characterize  $A^*$ . However, all the coefficients were computed to demonstrate that the homogenized material is isotropic (or quasi-isotropic). Herein, we use a linear material model with Young's modulus  $\mathbf{E} = 12 \times 10^9 \text{ Nm}^{-2}$  (i.e., 12GPa) and Poisson's ratio  $\nu = 0.35$ . We recall that, if the effective tensor  $A^*$  is isotropic, it can be written as:

$$A^* = 2\mu^* I_{2N} + \left(\kappa^* - \frac{2\mu^*}{N}\right) I_N \otimes I_N, \quad (9)$$

where  $\kappa^*$  and  $\mu^*$  are the bulk and shear moduli of the homogenized Hooke's law  $A^*$ , with its first Lamé coefficient defined by:  $\lambda^* = \kappa^* - \frac{2\mu^*}{N}$ .  $I_{2N}$  and  $I_N$  in (9), represent the fourth order symmetric identity and the identity tensor

of order  $N$ . The entries are defined by:

$$\begin{cases} \mu^* = A_{ijij}^* \\ \lambda^* = A_{iijj}^* \\ \kappa^* = A_{iijj}^* + \frac{2}{N} A_{ijij}^* \end{cases} \quad \forall i, j \in \{1, \dots, N\} \quad (10)$$

where the isotropy of  $A^*$  is satisfied if we have the following relations:

$$\forall i, j, k, l \in \{1, \dots, N\} \quad \begin{cases} A_{ijkl}^* = A_{klij}^* \\ A_{iijj}^* = 0 \\ A_{iiii}^* = A_{jjjj}^* \\ A_{iijj}^* = A_{kkll}^*; \quad \forall i \neq j, k \neq l \\ A_{iiii}^* = A_{ijij}^* + A_{iijj}^* \end{cases} \quad (11)$$

## Numerical results

The homogenized tensor  $A^*(\theta)$  has been computed for both periodic cells, for discrete values  $(\theta_i)_{i=1, \dots, n}$  of  $\theta$ : a preprocessing stage, which is performed offline. Herein, a table of the size  $n = 1000$  is built, which is then used to compute the local composites during the optimization process: a linear interpolation approach is used to update the homogenized tensor. The errors with respect to the equalities in (11) are depicted on Fig. 5 and Fig. 6.

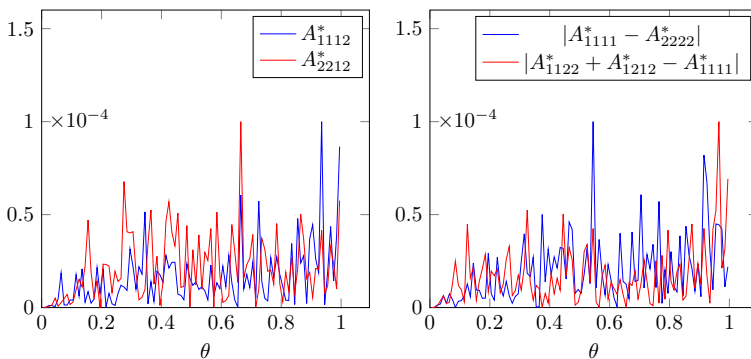


**Fig. 5** The errors with respect to the equalities in (11) for the smooth honeycomb

We note that, the residuals with respect to the equalities in (11), for the smooth honeycomb (Fig. 5) and the Kelvin foam (Fig. 6) are sufficiently small, which validates the isotropy assumption: the errors are less than  $10^{-4}$ .

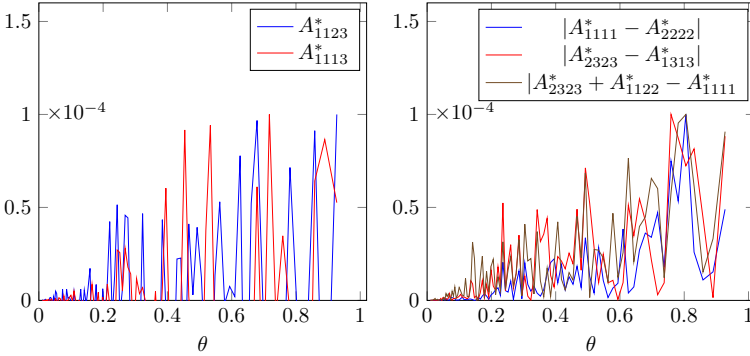


**Fig. 6** The errors with respect to the equalities in (11) for the Kelvin foam

### 2.3 Cell problem and homogenized model in conductivity

We now consider a general model problem of thermal or pressure conductivity, similar to the elasticity system defined in (2.2). Starting from a microscopic description of a problem, one seeks a macroscopic or effective model problem in conductivity  $K^*$  which can either be the permeability of a fluid flowing through a porous material or a problem of thermal conductivity through a two-phase material composed of solid and fluid one. We introduce the so-called cell problems, similar to the elasticity system. However, since the considered cell  $Y$  is isotropic, only one of its coefficient (e.g.,  $(K^*)_{11}$ ) could be computed in order to fully characterize  $K^*$ .

Let  $(e_i)_{i=1,\dots,N}$  be the canonical basis of  $\mathbb{R}^N$  and, for each unit vector  $e_i$ , we consider the following conductivity problem in the periodic cell  $Y$ :

$$\begin{cases} -\operatorname{div}(K(e_i + \nabla w_i)) = 0 & \text{in } Y \\ y \mapsto w_i(y) & Y \text{ periodic,} \end{cases} \quad (12)$$

where  $w_i(y)$  is the local variation of pressure created by an averaged (or macroscopic) gradient  $e_i$ . The homogenized conductivity  $K^*$  is then given in terms of the correctors  $w_i$  (solutions of (12)), defined by:

$$(K^*)_{ij} = \frac{1}{|Y|} \int_Y K(e_i + \nabla w_i) : (e_j + \nabla w_j) dy \quad \forall i, j \in \{1, 2\} \quad (13)$$

where the tensor  $K^*$  describes the effective or homogenized properties of the heterogeneous microstructure of periodic size  $\epsilon$ . We recall that,  $K^*$  does not depend on the choice of domain  $\Omega$ , source term  $f_f$ , or boundary conditions and,  $Y = Y_0 \cup (Y \setminus Y_0)$  is a disjoint reunion of the solid phase and void, where in thermal conductivity,  $K$  can be defined by:

$$K(y) = \begin{cases} k_s & \text{in } y \in Y_0 \\ k_f & \text{in } y \in Y \setminus Y_0 \end{cases} \quad (14)$$

wherein,  $k_s$  and  $k_f$  are some fixed constants thermal conductivity inside the solid and void. Though, in pressure conductivity,  $K$  is some fixed constant:

$$K(y) = \begin{cases} \epsilon_0 & \text{in } y \in Y_0 \\ 1 & \text{in } y \in Y \setminus Y_0 \end{cases} \quad (15)$$

where  $\epsilon_0$  is a given threshold.

## Numerical results

The tensor  $K^*$  has been computed for the smooth honeycomb for discrete values of  $\theta$ . For this latter, note that  $K^*$  is a matrix of order  $N$ , proportional to the identity matrix:

$$K^* = \alpha^* I_N, \quad \text{where } \alpha^* = (K^*)_{11} = (K^*)_{22},$$

because the chosen local cell is isotropic and, as a consequence,  $K^*$  can be identified to the scalar  $\alpha^*$ .

On Fig. 7, we plot the homogenized flow  $\frac{\alpha^*}{\|\alpha^*\|_\infty}$  (which is normalized), in comparison to the defined flow coefficient  $K_D^*(\theta) = \min\left(\frac{\epsilon_0 + (1-\epsilon_0)(1-\theta)}{\theta}, K_\infty\right)$  for discrete values  $(\theta_i)_{i=1, \dots, n}$ , with  $\|\alpha^*\|_\infty = \sup_{\theta_i} \alpha^*(\theta_i)$ ; see Section 3.1, for more details.

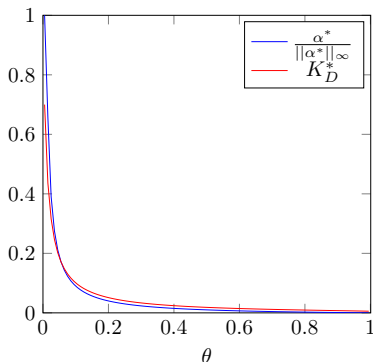


**Fig. 7** The homogenized flow  $\frac{\alpha^*}{\|\alpha^*\|_\infty}$  compared to the determined flow  $K_D^*$ , for different values of the density  $\theta$

As expected,  $\frac{\alpha^*}{\|\alpha^*\|_\infty}$  is a decreasing function with respect to the density  $\theta$ . We emphasize that, the residuals  $|(K^*)_{11} - (K^*)_{22}| \leq 10^{-6}$  and  $(K^*)_{12} \leq 10^{-3}$  are sufficiently small, which validates the isotropy assumption. We note that, the homogenized flow coefficient  $\frac{\alpha^*}{\|\alpha^*\|_\infty}$  can be approximated by the determined

flow coefficient  $K_D^*$ . Note that the above result remain valid for the Kelvin foam (i.e., the tetrakaidecahedron cell in 3-D).

### 3 Setting of the three-physic problem

Here, we investigate the weakly coupled model of heat propagation, fluid flow and structure deformation. First, the fluid flow is described using the Biot-Darcy's law, second, the heat propagation is characterized using the convection-diffusion equation and third, the three-physic problem is described by the linearized poro-thermo elasticity system, for the mechanical displacement.

Let  $\Omega$  be a fixed domain in  $\mathbb{R}^N$  ( $N = 2$  or  $3$ ), filled with composite material periodically perforated by the hexagonal cell in 2-D or tetrakaidecahedron cell in 3-D and, characterized by one parameter  $\theta$ : the material density, which is to be optimized. Let  $\mathbf{n}$  be the normal vector to the boundary  $\partial\Omega$ , pointing outward to the domain  $\Omega$ . The domain  $\Omega$  is described by three physical variables which are governed by three coupled models, that are:

- the motion of the fluid inside the domain  $\Omega$  described by the pressure field  $p$ , satisfying the Biot-Darcy's law
- the diffusion of heat inside the whole domain  $\Omega$ , and its transport by convection in the fluid domain, resulting in a temperature field  $T$ ;
- the deformation of the solid phase, as a result of the stress exerted by the fluid part and of the dilation induced by thermoelastic effects, characterized by a mechanical displacement  $u$

The physical equations chosen for the modeling of the state variables  $p$ ,  $T$  and  $u$  with their relevant set of boundary conditions are now described in strong form in Section 3.1, Section 3.2 and Section 3.3.

#### 3.1 Hydraulic law of Biot-Darcy-type for the pressure variable

We give a precise account of the weakly coupled fluid model that is based on the Biot-Darcy's law; the effect of which is to establish the pressure field as a function of material density  $\theta$ .

From a fluid point of view, Darcy's law describes the fluid ability to flow through a porous media such as soil, sandstone or rock; it states that, the fluid flowing through a unit area is directly proportional to the pressure drop per unit length  $\nabla p$  and, inversely, that the resistance of the porous medium is proportional to the flow  $\mu$  ([34]), which is defined by:

$$\mathbf{q} := -\frac{\kappa_f}{\mu_f} \nabla p = -K_D^* \nabla p, \quad (16)$$

where  $\mathbf{q}$ ,  $\kappa_f$ ,  $\mu_f$ ,  $\nabla p$ , and  $K_D^*$  characterize the flux ( $kgm^2s^{-1}$ ), permeability ( $m^2$ ), fluid viscosity ( $Nm^{-2}s$ ), pressure gradient ( $Nm^{-3}$ ), and the flow coefficient ( $m^4N^{-1}s^{-1}$ ) (which defines the fluid ability to flow through a porous medium). In order to smoothly and continuously distribute the pressure drop in fluid domain and differentiate between solid and void phase in the whole domain, the homogenized flow coefficient  $K^*(\theta(x))$  (which we numerically compute, see Section 2.3) is approximated by a smooth function, that is:

$$K_D^*(\theta(x)) := \min \left( \frac{\epsilon_0 + (1 - \epsilon_0)(1 - \theta(x))}{\theta(x)}, K_\infty \right), \quad (17)$$

where  $\epsilon_0$  and  $K_\infty$  are given thresholds, i.e.,  $\epsilon_0 = 10^{-4}$ ,  $K_\infty = 10^3$ . We recall that an homogenization method was performed on the flow coefficient and we notice that, the homogenized flow coefficient  $K^*$  can be characterized by the above function; see Fig. 7. We now assume that the density-dependent pressure field  $p$ , satisfies a Biot's law, defined by:

$$p := Mm - Mbe_{vol}, \quad (18)$$

where  $M$ ,  $m$  and  $e_{vol}$  are smooth enough functions related to the material density  $\theta$ , defined by:

$$m(\theta) := (1 - \theta)\rho, \quad M(\theta) := \frac{1 - \theta}{\kappa_v} - \frac{b(\theta) - (1 - \theta)}{\kappa_s}, \quad e_{vol} := div(u), \quad (19)$$

where  $\rho$ ,  $\kappa_v$ ,  $\kappa_s$ , and  $e_{vol}$ , represent the density of the flux, compressibility of the void, the solid phase, and the volume variation of the solid phase at each finite element; the parameters  $M$  and  $b$  are the so called Biot modulus and Biot coefficient. The Biot's law (18) is assumed to be related to Darcy's law (16) by:

$$\mathbf{q} := mv_f = -K_D^* \nabla p, \quad (20)$$

where  $v_f$  represents the velocity of the flux. Thus, the above equation (20), allows to render gradually the pressure drop from the inner pressure boundary to the outer pressure boundary. Note that, this penetrating pressure of Biot-Darcy's law is similar to that introduced in [21], which makes this pressure loading boundary a smeared-out version of an applied pressure load on a sharp boundary. In addition to the Biot-Darcy equation (20), we assume that the state equation satisfies the law of conservation of mass in view of incompressible fluid, that is:

$$\frac{\partial m}{\partial t} := -div(\mathbf{q}) = div(K_D^* \nabla p) \quad (21)$$

Consequently, we derive from the Biot's law (20), the equation:

$$\frac{\partial p}{\partial t} := M(\theta(x)) \frac{\partial m}{\partial t} - M(\theta(x))b(\theta(x)) \frac{\partial e_{vol}}{\partial t}, \quad (22)$$

and for sake of simplicity, we assume that our fluid model is stationary and satisfies the law of conservation of mass (in view of incompressible fluid), that is:

$$\frac{\partial m}{\partial t} := -\operatorname{div}(\mathbf{q}) = \operatorname{div}(K_D^* \nabla p) = 0 \quad (23)$$

We now assume that our design domain is filled with isotropic composite material and as such, the Biot's coefficient  $b(\theta)$  can be defined by:

$$b(\theta(x)) := 1 - \frac{\kappa_s(\theta(x))}{\kappa}, \quad (24)$$

where,  $\kappa$  and  $\kappa_s(\theta(x))$  represent the bulk moduli of the solid phase  $A$  and the homogenized tensor  $A^*(x)$ . Note that  $A^*(x)$  tends to  $A$ , when  $\theta(x)$  tends to 1; thus,  $\kappa_s(\theta)$  tends to  $\kappa$ ; this article should be approached within such background, that is, we assume that the weakly coupled fluid model is defined in the particular case of a porous isotropic medium. Note that the Biot modulus (19) and coefficient (24) are explicitly defined only in the case of a linear isotropic elastic matrix microscopically homogeneous which is the case herein. By using the Biot-Darcy's law (23), the weakly coupled fluid model can be defined by:

$$\text{(Biot-Darcy)} \begin{cases} -\operatorname{div}(K_D^* \nabla p) = 0 & \text{in } \Omega, \\ p = p_0 & \text{on } \Gamma_D^f, \\ \mathbf{q}_\Gamma \cdot \mathbf{n} = f_f & \text{on } \Gamma_N^f, \\ \mathbf{q}_\Gamma \cdot \mathbf{n} = 0 & \text{on } \Gamma^f = \partial\Omega \setminus (\Gamma_D^f \cup \Gamma_N^f), \end{cases} \quad (25)$$

In (25),  $f_f$  is an applied Neumann isoflux condition for the pressure variable  $p$ . The boundary of the fluid phase is the disjoint reunion

$$\partial\Omega = \Gamma_D^f \cup \Gamma_N^f \cup \Gamma^f$$

of a Dirichlet (or inlet) part  $\Gamma_D^f$  where the flow enters with a given pressure  $p = p_0$ , a Neumann (or outlet) part  $\Gamma_N^f$  where normal stress is imposed, and free interface  $\Gamma^f$  of  $\partial\Omega$ . At this stage it is assumed that the deformation of the solid domain is sufficiently small so that no slip boundary conditions hold on:  $\mathbf{q}_\Gamma \cdot \mathbf{n} = 0$ . Therefore, the variable  $p$  depends solely on the material density  $\theta(x)$ , for all  $x \in \Omega$ .

### 3.2 Convection-diffusion for the temperature variable

We give a precise account of the weakly coupled diffusion of the heat model, that is based on the convection-diffusion equation: the fluid velocity  $v_f$  determines the physical behavior of the temperature  $T$  in the whole domain, as a result of convection and diffusion effects inside the fluid domain and of pure diffusion inside the solid domain; see [35], for references.



Assume that, when  $\epsilon$  tends to 0, the periodic microstructure  $\Omega_\epsilon$  tends to an homogeneous domain  $\Omega$ , filled with fine mixtures of solid and void phase; let  $k^*$  denote the homogenized thermal conductivity inside the porous media (which we numerically computed, see Section 2.3), and let  $c_p$  be the thermal capacity of the fluid. Then, the weakly coupled diffusion of the heat model is defined by the convection-diffusion equation, that is:

$$\begin{cases} -\operatorname{div}(k^*\nabla T) + \phi(\rho c_p)_f v_f \nabla T = 0 & \text{in } \Omega, \\ T = T_0 & \text{on } \Gamma_T^D, \\ -k^* \frac{\partial T}{\partial \mathbf{n}} = h & \text{on } \Gamma_T^N, \\ -k^* \frac{\partial T}{\partial \mathbf{n}} = 0 & \text{on } \Gamma^T \end{cases} \quad (26)$$

where, we use the subscripts  $f$  for the restriction to fluid phase in  $\Omega$ . The boundary  $\partial\Omega = \Gamma_T^D \cup \Gamma_T^N \cup \Gamma^T$  is split into a Dirichlet part, where a temperature  $T_0$  is imposed on  $\Gamma_T^D$ , a Neumann part where a given incoming heat flux  $h$  is applied on  $\Gamma_T^N$  and free interface  $\Gamma^T$ . The convection-diffusion equation (26) is now recast as thermal Biot-Darcy equation, that is:

$$\begin{cases} -\operatorname{div}(k^*\nabla T) + (-c_p K_D^* \nabla p)_f \nabla T = 0 & \text{in } \Omega, \\ T = T_0 & \text{on } \Gamma_T^D, \\ -k^* \frac{\partial T}{\partial \mathbf{n}} = h & \text{on } \Gamma_T^N, \\ -k^* \frac{\partial T}{\partial \mathbf{n}} = 0 & \text{on } \Gamma^T \end{cases} \quad (27)$$

where  $\phi \rho v_f = m v_f = -K_D^* \nabla p$  satisfies the Darcy law (25). As a consequence, the convection-diffusion model is defined by (27), which we assumed stationary. Similar to the Biot-Darcy model (25), starting from a microscopic description of a problem, one seeks a macroscopic or effective model problem in conductivity. We consider a model problem of thermal flow in a periodic medium: an heterogeneous domain obtained by mixing periodically two different phases, one being the solid phase and the other being the void inclusions; and as it has been seen in Section 2, to compute the homogenized conductivity tensor  $k^*$ , we introduce the so-called cell problems, and since the considered cell  $Y$  is specifically chosen in order to design isotropic composites, only one of its coefficient (e.g.,  $(k^*)_{11}$ ) could be computed in order to fully characterized  $k^*$ , a scalar value.

### 3.3 Elasticity with fluid-structure interaction

Finally, the pressure variable  $p$  and the temperature  $T$  together determine the displacement  $u$  of the solid phase in  $\Omega$ , which we assume to be isotropic thermoelastic composite material, with homogenized Lamé coefficients denoted  $\lambda^*$ ,  $\mu^*$ . Let  $\alpha$  be the thermal expansion parameter and  $T_{ref}$  be the temperature at rest; then, the weakly coupled thermal fluid-elastic model is defined by the

linear thermo-elasticity (of Biot-Coussy type):

$$\begin{cases} -\operatorname{div}(\sigma(u, T)) = -b\nabla p & \text{in } \Omega, \\ u = u_0 & \text{on } \Gamma_D^s, \\ \sigma(u, T) \cdot \mathbf{n} = f_s & \text{on } \Gamma_N^s, \\ \sigma(u, T) \cdot \mathbf{n} = 0 & \text{on } \Gamma^s, \end{cases} \quad (28)$$

where the homogenized stress tensor is defined as follows:

$$\sigma(u, T) = A^*(e(u) - \alpha(T_s - T_{ref})I) \quad \text{with } A^*e(u) = 2\mu^*e(u) + \lambda^*\operatorname{Tr}(e(u))I, \quad (29)$$

$I$  is the identity matrix. Note that, the source term in (28) is the stress exerted by the fluid part; the boundary  $\partial\Omega$  is split into a Dirichlet part  $\Gamma_D^s$  where a displacement  $u = u_0$  is prescribed, a Neumann part  $\Gamma_N^s$  where a stress  $f_s$  is imposed and, a free part  $\Gamma^s$ .

*Remark 1* The above model is a simplified version of a genuine thermal fluid-solid coupling between the solid and fluid phases. A more accurate description of fluid-structure interaction would feature a transition regime and inertia regime:

$$\mathbf{q} := mv_f + \rho C_{for} v_f^2$$

where  $C_{for}$  is an inertia parameter of the fluid flow, called Forchheimer coefficient. However, for sake of simplicity, we opted for simplified version, which is justifiable insofar as we wish to obtain a first qualitative result of microstructure without however sizing as accurately as possible the system. Hence, the Forchheimer coefficient  $C_{for}$  is neglected in (27).

Thanks to this simplification, the system (3.1), (27) and (3.3) are only weakly coupled: its resolution is achieved by solving the fluid system (25), then using the fluid stress resulting from the pressure  $p$  in the heat transfer equation (27), and finally using the fluid stress and the temperature  $T$  to solve the linear poro-thermo elasticity (28).

## 4 The optimization problem formulation and its sensitivity analysis

We present the optimization problem formulation associated to the weakly coupled three-physic problem and discuss the sensitivity analysis for such design problems. The announced goal is the resolution of relaxed unconstrained version of the original optimization problem, that is:

$$\begin{aligned} & \min_{\theta} J^*(\theta, p(\theta), T(\theta), u(\theta)) \\ \text{s.t. } & \begin{cases} g_i(\theta, p(\theta), u(\theta)) = 0, & 1 \leq i \leq p, \\ h_j(\theta, p(\theta), u(\theta)) \leq 0, & 1 \leq j \leq q, \end{cases} \end{aligned} \quad (30)$$

where  $J^*$ ,  $g_i$  and  $h_j$  are arbitrary relaxed shape objective and constraint functionals. For its resolution, we shall rely on the alternate minimization algorithm detailed in Section 5.1, which (like any other first order optimization method) requires to compute the sensitivity of the above functionals: here, the adjoint-state method [1] is used to determine the sensitivities of the objective functions and constraints with respect to the design variable  $\theta$ . It is worth to mention that, likewise in [23], the authors employed the adjoint-state method to evaluate the sensitivities of objective functions (constituted by the Biot model coefficients with respect to the underlying pore shape described by a B-spline box which embeds the whole representative cell) and the gradient-based method to solve the optimization problems; howbeit, the considered shape derivatives of the homogenized coefficients are different: they rely on the shape sensitivity technique and the material derivative approach. Herein, the "shape" is describe by the density  $\theta$  and, the shape derivatives are performed using the Lagrangian method and the projected gradient algorithm. In this context, this means computing the derivative of the mapping:

$$\theta \mapsto J^*(\theta, p(\theta), T(\theta), u(\theta)),$$

where we recall that  $\theta$  belongs in general to the set of admissible design variables  $\mathcal{U}_{ad}$ , that is:

$$\mathcal{U}_{ad} := \left\{ \theta \in L^\infty(\Omega; \mathbb{R}_+^*) \mid \theta(x) \in [0, 1], \forall x \in \Omega \right\}$$

In contrast, in [23], a general optimization variable  $\alpha$  is introduced which is related to the effective medium parameters: it determines the homogenized coefficients for any position  $x \in \Omega$ .

## 4.1 A fully Lagrangian setting for the sensitivity analysis

Although very common and widely used in the literature, an issue with the adjoint-state method [1, 9] is that the computation of the derivatives depend very much on the assumptions made on the nature of the considered objective functional  $J^*$  (different type of functionals may lead to different strong forms for the adjoint equations, where this fact is exemplified), which imposes to redo the analytical derivation whenever the objective function is modified, and to update the numerical implementation accordingly. Here, we use a fully Lagrangian setting to compute rigorously the derivative of very general objective functionals in the simplified setting of Section (3.1) to Section (3.3). The sensitivities of the state variables  $p(\theta)$ ,  $T(\theta)$  and  $u(\theta)$  are calculated first, in order to obtain the derivative of an arbitrary objective functional in volume form. Then, under sufficient regularity assumptions, the well-known adjoint variable method together with suitable augmented Lagrangian functional yield general derivative formulas.

## 4.2 A modified objective functional and Lagrangian derivative

In a gradient-based topology optimization, it is essential to determine sensitivities of the objective functional and the constraints with respect to the design variable(s). The starting remark is that the relaxed functional  $J^*$ , although appearing naturally in the formulation of the optimization problem (30) is not so convenient for the mathematical analysis. Indeed, the domain of definition of  $J^*(\theta, \dots, \dots)$  is a functional space which depends on the first argument  $\theta$ . In order to discuss the precise mathematical settings of this three-physic problem, we introduce the functional spaces which are required, that are:

$$\begin{aligned} V(\Gamma_D^f) &= \{q \in H^1(\Omega) \mid q = 0 \text{ on } \Gamma_D^f\}, \text{ for the pressure variable } p \\ V(\Gamma_T^D) &= \{S \in H^1(\Omega) \mid S = 0 \text{ on } \Gamma_T^D\}, \text{ for temperature variable } T \\ V(\Gamma_D^s) &= \{v \in H^1(\Omega)^N \mid v = 0 \text{ on } \Gamma_D^s\}, \text{ for the displacement } u \end{aligned} \quad (31)$$

and, we consider the subspace

$$H^{1/2}(\Gamma_N^s) = \{v|_{\Gamma_N^s} \mid v \in V(\Gamma_D^s)\}$$

and its dual space  $H^{-1/2}(\Gamma_N^s)$ ; as well the affine spaces associated to the non-homogeneous Dirichlet boundary data  $u_0 \in H^{1/2}(\Gamma_D^s; \mathbb{R}^N)$ ,  $p_0 \in H^{1/2}(\Gamma_D^f; \mathbb{R})$  and  $T_0 \in H^{1/2}(\Gamma_T^D; \mathbb{R})$  featured in (3.1) to (3.3). The state variables  $p$ ,  $T$  and  $u$  are then solutions to the following variational problems: find  $(p, T, u) \in \{p_0 + V(\Gamma_D^f), T_0 + V(\Gamma_T^D), u_0 + V(\Gamma_D^s)\}$  such that,

$$\begin{cases} \int_{\Omega} K_D^* \nabla p \cdot \nabla q + \int_{\Gamma_N^f} f_f q \, dx = 0, & \forall q \in V(\Gamma_D^f), \\ \int_{\Omega} k^* \nabla T \cdot \nabla S \, dx + \int_{\Gamma_T^D} h S \, ds + \int_{\Omega} (-c_p S K_D^* \nabla p) \cdot \nabla T \, dx = 0, & \forall S \in V(\Gamma_T^D), \\ \int_{\Omega} \sigma(u, T_s) e(v) \, dx - \int_{\Gamma_N^s} f_s \cdot v \, ds + \int_{\Omega} b \nabla p \cdot v \, dx = 0, & \forall v \in V(\Gamma_D^s) \end{cases} \quad (32)$$

*Remark 2* Let us comment on the well-posedness of the coupled system of variational problems in (32). The volumic source terms are assumed to enjoy  $H^1$  regularity in the domain. The surface fluxes  $h$  and  $f_s$  in (27) and (28) are assumed to belong to  $L^2$  spaces. The variational formulation of the thermal equation is not well-posed in utter generality because of the lack of coercivity induced by the advection term  $\int_{\Omega} (-c_p K^* \nabla p) \cdot \nabla T$  (27) and of the presence of in-homogeneous Dirichlet boundary conditions. Though, in usual applications (see [20], for reference), it is customary to impose a Dirichlet boundary condition  $T = T_{0,f}$  at the inlet of the computational domain (where  $-K_D^* \nabla p \cdot \mathbf{n} < 0$ ) and a Neumann boundary condition  $-k^* \nabla T \cdot \mathbf{n} = 0$ . This together with the incompressibility condition  $-\text{div}(K_D^* \nabla p) = 0$  is easily shown to imply the coercivity of the bilinear form featured in (32); see e.g. [1]. Eventually, the well-posedness of the linear elasticity problem results from the Lax-Milgram theorem. In the above context, we aim at solving the minimization problem

(30) where the pressure  $p(\theta)$ , temperature  $T(\theta)$  and elastic displacement  $u(\theta)$  are the solutions to (25), (27) and (28).

In order to address the sensitivity of an arbitrary objective function, the classical idea is to work within a Lagrangian framework. Therefore, we consider the corresponding Lagrangian, which is an augmented function of the objective function that is:

$$\begin{aligned} \mathcal{L}(\hat{\theta}, \hat{u}, \hat{\underline{u}}, \hat{p}, \hat{\underline{p}}, \hat{T}, \hat{\underline{T}}, \ell) &= J^*(\hat{\theta}) + \int_{\Omega} \hat{\underline{u}}(-div(\sigma(\hat{u}, \hat{T}) + b(\hat{\theta})\nabla\hat{p})) dx \\ &\quad + \int_{\Omega} \hat{T}(-div(k^*\nabla\hat{T}) - c_p K_D^* \nabla\hat{p} \cdot \nabla\hat{T}) \quad (33) \\ &\quad + \int_{\Omega} \hat{\underline{p}}(-div(K_D^*(\hat{\theta})\nabla\hat{p})) dx + \ell(\int_{\Omega} \hat{\theta} dx - \Theta), \end{aligned}$$

where,  $(\hat{\theta}, \hat{u}, \hat{\underline{u}}, \hat{p}, \hat{\underline{p}}, \hat{T}, \hat{\underline{T}}) \in L^\infty(\Omega) \times H_0^1(\Omega; \mathbb{R}^N)^2 \times H_0^1(\Omega; \mathbb{R})^2 \times H_0^1(\Omega; \mathbb{R})^2$  are independent variables; the positive scalar  $\ell$  is the Lagrange multiplier designed to satisfy the volume constraint. Note that the objective function  $J^*(\hat{\theta})$  depends upon the state variables  $u$ ,  $p$  and  $T$ . By integration by parts, we get:

$$\begin{aligned} \mathcal{L}(\hat{\theta}, \hat{u}, \hat{\underline{u}}, \hat{p}, \hat{\underline{p}}, \hat{T}, \hat{\underline{T}}, \ell) &= J^*(\hat{\theta}) + \int_{\Omega} (\sigma(\hat{u}, \hat{T}) : e(\hat{\underline{u}}) + b(\hat{\theta})\nabla\hat{p} \cdot \hat{\underline{u}}) dx \\ &+ \int_{\Omega} k^*\nabla\hat{T} \cdot \nabla\hat{\underline{T}} - \int_{\Omega} c_p \hat{\underline{T}} K_D^* \nabla\hat{p} \cdot \nabla\hat{T} + \int_{\Omega} K_D^* \nabla\hat{p} \cdot \nabla\hat{\underline{p}} dx + \ell(\int_{\Omega} \hat{\theta} dx - \Theta), \quad (34) \end{aligned}$$

where again, we point out that  $J^*$  is assumed to be a "smooth" enough function, otherwise we cannot apply the adjoint-state method [1, 9].

### 4.3 Sensitivity analysis for the three-physic problem

The sensitivities are evaluated by differentiating the Lagrangian (34) with respect to state variables  $u$ ,  $p$  and  $T$  in directions  $\phi_u \in H^1(\Omega)^N$ ,  $\phi_p \in H^1(\Omega)$  and  $\phi_T \in H^1(\Omega)$ . Let  $(u, \underline{u}) \in H_0^1(\Omega; \mathbb{R}^N)^2$  be a stationary point of  $\mathcal{L}$ . Then, the derivative of the Lagrangian (34) with respect to  $u$ , in direction  $\phi_u \in H^1(\Omega)^N$  is given by:

$$\left\langle \frac{\mathcal{L}}{\partial u}, \phi_u \right\rangle = \left\langle \frac{\partial J^*}{\partial u}, \phi_u \right\rangle + \int_{\Omega} \left\langle \frac{\partial \sigma(\hat{u}, \hat{T})}{\partial u}, \phi_u \right\rangle : e(\hat{\underline{u}}) dx, \quad (35)$$

while the derivative with respect to  $p$ , in direction  $\phi_p \in H^1(\Omega)$  is given by:

$$\begin{aligned} \left\langle \frac{\mathcal{L}}{\partial p}, \phi_p \right\rangle = & \left\langle \frac{\partial J^*}{\partial p}, \phi_p \right\rangle + \int_{\Omega} b \nabla \phi_p \cdot \hat{u} \, dx + \int_{\Omega} (-c_p \hat{T} K_D^* \nabla \phi_p) \nabla \hat{T} \\ & + \int_{\Omega} K_D^* \nabla \phi_p \cdot \nabla \hat{p} \, dx \end{aligned} \quad (36)$$

and, the derivative with respect to  $T$ , in direction  $\phi_T \in H^1(\Omega)$  is given by:

$$\begin{aligned} \left\langle \frac{\mathcal{L}}{\partial T}, \phi_T \right\rangle = & \left\langle \frac{\partial J^*}{\partial T}, \phi_T \right\rangle + \int_{\Omega} \left\langle \frac{\partial \sigma}{\partial T}, \phi_T \right\rangle : e(\hat{u}) \, dx + \int_{\Omega} k^* \nabla(\phi_T) \cdot \nabla \hat{T} \, dx \\ & + \int_{\Omega} (-c_p \hat{T} K_D^* \nabla \hat{p}) \nabla(\phi_T) \, dx, \end{aligned} \quad (37)$$

which when equations (35), (36) and (37) vanish are nothing more than the variational formulation associated to the adjoint-states. Moreover, the derivatives with respect  $\underline{u}$ ,  $\underline{p}$  and  $\underline{T}$ , in directions  $\phi_u \in H^1(\Omega)^2$ ,  $\phi_p \in H^1(\Omega)$  and  $\phi_T \in H^1(\Omega)$  are simply the state equations:

$$\left\langle \frac{\partial \mathcal{L}}{\partial \underline{u}}, \phi_u \right\rangle = \int_{\Omega} (\sigma(\hat{u}, \hat{T}) : e(\phi_u) + b(\hat{\theta}) \nabla \hat{p} \cdot \phi_u) \, dx, \quad (38)$$

$$\left\langle \frac{\partial \mathcal{L}}{\partial \underline{p}}, \phi_p \right\rangle = \int_{\Omega} K_D^* \nabla \hat{p} \cdot \nabla \phi_p \, dx, \quad (39)$$

and

$$\left\langle \frac{\partial \mathcal{L}}{\partial \underline{T}}, \phi_T \right\rangle = \int_{\Omega} k^* \nabla \hat{T} \cdot \nabla \phi_T + \int_{\Omega} (-c_p \phi_T K_D^* \nabla \hat{p}) \nabla \hat{T} \, dx, \quad (40)$$

which when equation (38), (39) and (40) vanish is nothing more than the variational formulation associated to the state equations: note that to obtain the adjoint-state equations in [23], the optimality condition for the state variables is considered and, together with the state variables yield the adjoint state variables. Finally, the partial derivative of the Lagrangian  $\mathcal{L}$  with respect to  $\theta$ , in direction  $\bar{\theta} \in L^\infty(\Omega; \mathbb{R})$  at the stationary point  $(u, \underline{u}, p, \underline{p}, T, \underline{T})$  is given by:

$$\begin{aligned} \left\langle \frac{d\mathcal{L}}{d\theta}, \bar{\theta} \right\rangle = & \left\langle \frac{\partial J^*}{\partial \theta}, \bar{\theta} \right\rangle + \int_{\Omega} \left( \frac{\partial \sigma}{\partial \theta} : e(\hat{u}) + \frac{\partial b}{\partial \theta} \nabla \hat{p} \cdot \hat{u} + \frac{\partial K_D^*}{\partial \theta} \nabla \hat{p} \cdot \nabla \hat{p} \right. \\ & \left. + \frac{\partial k^*}{\partial \theta} \nabla \hat{T} \cdot \nabla \hat{T} + (-c_p \hat{T} \frac{\partial K_D^*}{\partial \theta} \nabla \hat{p}) \nabla \hat{T} + \ell \right) \bar{\theta} \, dx \end{aligned} \quad (41)$$

Note that, Eq. (41) is defined using the adjoint-state method. As a consequence, the descent direction  $\bar{\theta} = d\theta$  is defined by solving Eq. (41). The term

$\langle \frac{\partial J^*}{\partial \bar{\theta}}, \bar{\theta} \rangle$  is the partial derivative of the objective function  $J^*$  with respect to  $\bar{\theta}$ , in direction  $\bar{\theta}$ , while the term

$$\int_{\Omega} \left( \frac{\partial \sigma}{\partial \theta} : e(\hat{\underline{u}}) + \frac{\partial b}{\partial \theta} \nabla \hat{p} \cdot \hat{\underline{u}} + \frac{\partial K_D^*}{\partial \theta} \nabla \hat{p} \cdot \nabla \hat{p} + \frac{\partial k^*}{\partial \theta} \nabla \hat{T} \cdot \nabla \hat{T} \right. \\ \left. + (-c_p \hat{T} \frac{\partial K_D^*}{\partial \theta} \nabla \hat{p}) \cdot \nabla \hat{T} + \ell \right) \bar{\theta} dx$$

is the adjoint.  $\hat{\underline{u}}$ ,  $\hat{p}$  and  $\hat{T}$  are the adjoint-state variables, solutions to the adjoint equations (35)-(37) (which we have to solve first). We recall that  $\ell$  is the Lagrange multiplier designed to satisfy the volume constraint at each iteration and, such a constraint is routinely handled in elementary calculus of variations: here, the dichotomy approach is employed.

## 5 Topology optimization of modulated periodic composite materials

Here, our numerical algorithm is proposed; we describe how the methodology applies to the weakly coupled three physics system of (25-28).

### 5.1 Alternate minimization method

The problem (30) is solved using the alternate minimization algorithm.

#### 5.1.1 Minimizing over the stress field

For given design field  $\theta$ , the minimization with respect to the stress field  $\sigma$  amounts to solve the poro-linear thermoelasticity problem (28), with a material of elasticity tensor equal to  $A^*(x)$  in  $\Omega$  and where, the design  $(\theta, A^*)$  is computed by linear interpolation over a surrogate model of  $A^*(\theta)$ : a preprocessing stage, which is performed offline; see Section 2.2.

#### 5.1.2 Minimizing over the density field

The minimization over the density field  $\theta$  for a given stress tensor  $\sigma$ , is performed using the projected gradient algorithm and, as our problem (30) is not self-adjoint, one needs to define the associated adjoint problem. As a consequence, the descend direction  $h = d\theta$  is defined by solving:

$$\left\langle \frac{\partial \mathcal{L}}{\partial \theta}, h \right\rangle = \left\langle \frac{\partial J^*}{\partial \theta}, h \right\rangle + \int_{\Omega} \left( \frac{\partial \sigma}{\partial \theta} : e(\underline{u}) + \left( \frac{\partial b}{\partial \theta} \nabla p \cdot \underline{u} \right) + \frac{\partial K_D^*}{\partial \theta} \nabla \hat{p} \cdot \nabla \hat{p} dx \right. \\ \left. + \frac{\partial k^*}{\partial \theta} \nabla T \cdot \nabla T + (-c_p \hat{T} \frac{\partial K_D^*}{\partial \theta} \nabla p) \nabla T + \ell \right) h dx, \quad (42)$$

where the descend direction  $h = d\theta$  has to satisfy the inequality

$$\left\langle \frac{\partial \mathcal{L}}{\partial \theta}(\theta, \underline{u}, \underline{u}, \underline{p}, \underline{p}, T, \underline{T}, \ell), d\theta \right\rangle < 0, \quad (43)$$

which is achieved by choosing

$$d\theta = - \left( \frac{\partial J_1^*}{\partial \theta}(\theta) + \frac{\partial \sigma}{\partial \theta} : e(\underline{u}) + \frac{\partial b}{\partial \theta} \nabla p \cdot \underline{u} + \frac{\partial K_D^*}{\partial \theta} \nabla \hat{p} \cdot \nabla \underline{\hat{p}} \, dx + \frac{\partial k^*}{\partial \theta} \nabla T \cdot \nabla \underline{T} \right. \\ \left. + (-c_p \underline{T} \frac{\partial K_D^*}{\partial \theta} \nabla p) \nabla T_f + \ell \right) \quad (44)$$

with  $\langle \frac{\partial J_1^*}{\partial \theta}, h \rangle = \int_{\Omega} \frac{\partial J_1^*}{\partial \theta} \cdot h \, dx$ . At iteration  $n$ , the optimal density  $\theta$  is then updated by performing the projected gradient:

$$\theta^{n+1} = P_{[0,1]}(\theta^n + \delta d\theta), \quad (45)$$

where  $\delta > 0$  is the step size and, in practice, we use an adaptive step size  $\delta$ : at each iteration, if the newly computed composite structure is accepted (that is, if the current objective function  $J^*(\theta^n)$  is lower than previous one  $J^*(\theta^{n-1})$ ), the step size  $\delta$  is increased of 20%, else if it is rejected, the step size is divided by 2.  $P_{[0,1]}$  is the projection operator on the interval  $[0, 1]$ . Numerically, the partial derivative of the Lagrangian  $\frac{\partial \mathcal{L}}{\partial \theta}$  is regularized using an equivalent  $H^1$ -norm, that is:

$$\int_{\Omega} \left( \frac{\partial \mathcal{L}}{\partial \theta} h + \eta^2 \nabla \frac{\partial \mathcal{L}}{\partial \theta} \cdot \nabla h \right) dx = \langle \frac{\partial J^*}{\partial \theta}, h \rangle + \int_{\Omega} \left( \left( \frac{\partial \sigma}{\partial \theta} : e(\underline{u}) + \frac{\partial b}{\partial \theta} \nabla p \cdot \underline{u} \right) \right. \\ \left. + \frac{\partial k^*}{\partial \theta} \nabla T \cdot \nabla \underline{T} + (-c_p \frac{\partial K_D^*}{\partial \theta} \nabla p) \nabla T \underline{T} + \ell \right) h \, dx, \quad (46)$$

where  $\eta$  is a small coefficient, which typically depends on the size of the elements of the mesh: thanks to this coefficient, we are able to numerically regularize the partial derivative on a length scale of order  $\eta$  and to limit the checkerboard effect on the density  $\theta$ .

### 5.1.3 Complete optimization algorithm.

The alternate directions algorithm is an iterative method, structured as follows:

1. Initialization of the design variable  $\theta$  such that :

$$\forall x \in \Omega, \quad \theta^0(x) = \frac{\Theta}{\int_{\Omega} 1 \, dx}$$



2. Iteration until convergence, for  $n \geq 0$  :
  - (a) Computation of the state variable  $p^n$  through the Biot-Darcy model (25), with the design  $(\theta^n, A^*(x))$
  - (b) Computation of the state variable  $T^n$  through the convection-diffusion equations (27), with the design  $(\theta^n, A^*(x))$
  - (c) Computation of the stress tensor  $\sigma^n$  through the linear poro-thermo elasticity problem (28), with the design shape  $(\theta^n, A^*(x))$  and descend direction  $d\theta^n$  for a given stress tensor  $\sigma^n$  using formulas (44)
  - (d) Updating the design variable  $\theta^{n+1}$  using formulas (45) for the descend direction  $d\theta^n$  and then updating the design  $(\theta^{n+1}, A^*(x))$ , by linear interpolation.

## 6 Numerical results and discussion

We introduce our numerical results in the three physics context detailed in Section 3. A variety of 2-D and 3-D test cases are presented to demonstrate that our alternate directions algorithm produces physically correct results. The algorithm (5.1.3) has been implemented in FreeFem++[38], where all the unknowns are discretized using  $P_1$  finite elements. For all our computations, a linear material model with Young's modulus  $\mathbf{E} = 12 \times 10^9 Nm^{-2}$  (12GPa) and Poisson's ratio  $\nu = 0.35$  are considered. The void (i.e.,  $\theta = 0$ ) is replaced with a very compliant material: the smallest admissible value of  $\theta$  is fixed at  $10^{-4}$ , in order to avoid singularities of the effective tensor when the elasticity problem is solved.

We propose five test cases, where four out of five are new to the best of our knowledge: the first three are 2-D examples and the last two are in 3-D. First, we propose a poro-mechanical problem (where the convection-diffusion model (27) is not taken into account), second, a convective heat transfer (where the linear elasticity model (28) is not taken into account), third, all the three physics are involved; and for the remaining two examples, we provide the 3-D analogue of the second and third examples.

### 6.1 A fluid-structure interaction problem

In this example, the bounding box of the structure is a square of dimension  $L$  ( $m$ ), fixed on the upper middle of the left-right side boundary  $\Gamma_D^s$ , on a zone of width  $\frac{L}{10}$ , while submitted to uniform traction load  $\mathbf{f}_s$  on a small portion of the upper-middle boundary  $\Gamma_N^s$ . In addition, a fluid of density  $\mathbf{q}_0$  ( $kgm^2s^{-1}$ ) is flowing through the left-middle side boundary  $\Gamma_N^f$ , while submitted to a pressure load  $p_0$  (bar) at the corresponding opposite side  $\Gamma_D^f$ . All the other boundaries are insulated from the outside: zero Neumann boundary conditions hold for the pressure; see Fig. 8 for a schematic of this test case.

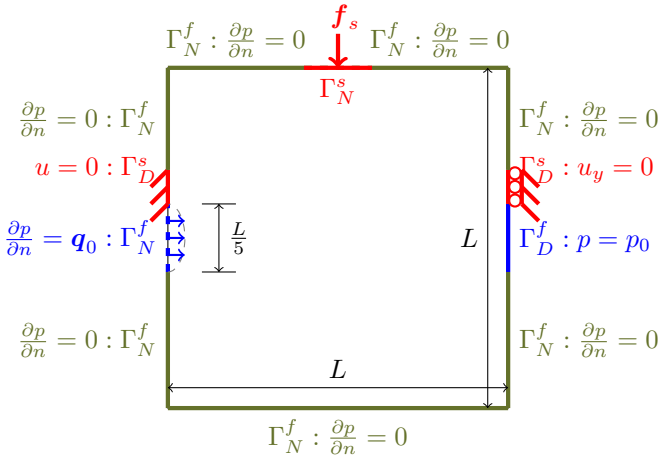


**Fig. 8** Setting for the fluid-structure interaction problem of Section 6.1

$L$	$q_0$	$p_0$
0.1	1.5	0

**Fig. 9** Numerical values of the physical parameters for test case of Section 6.1

We neglect the thermal effects (namely, Eq. (27) is ignored), so that (28), boils down to a poro-linear elasticity system with the forcing induced by the mechanical load and the fluid. Our aim is to achieve a trade-off between the minimization of the compliance of the solid body and the maximization of the hydraulic power transferred by the fluid, subjected to a volume constraint, that is:

$$\begin{aligned}
 J^*(\theta, p(\theta), u(\theta)) = & \underbrace{\omega \left( \int_{\Omega} A^* e(u) : e(u) \, dx \right)}_{\text{Elastic strain energy}} + (1 - \omega) \underbrace{\left( - \int_{\Omega} K^* \nabla p \cdot \nabla p \, dx \right)}_{\text{Hydraulic power}}, \\
 & \text{s.t. } \left\{ \frac{1}{|\Omega|} \int_{\Omega} \theta \, dx = \Theta \right. \\
 & \qquad \qquad \qquad (47)
 \end{aligned}$$

for some fixed coefficient  $\omega \in [0, 1]$ : it measures the relative weight given to each term in (47).

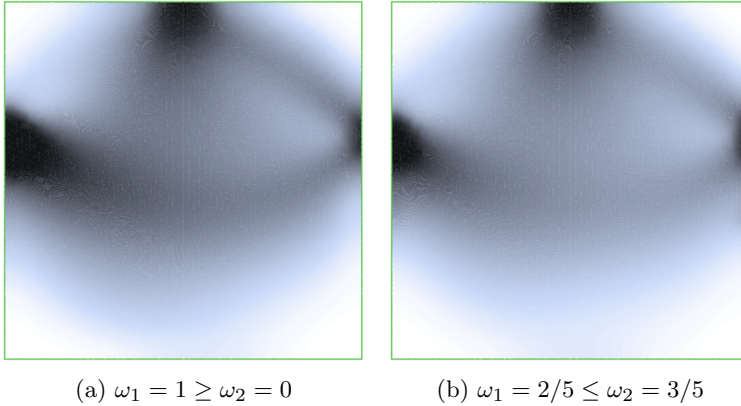


**Fig. 10** The optimal density for the two-physic problem of Section 6.1, in both situations

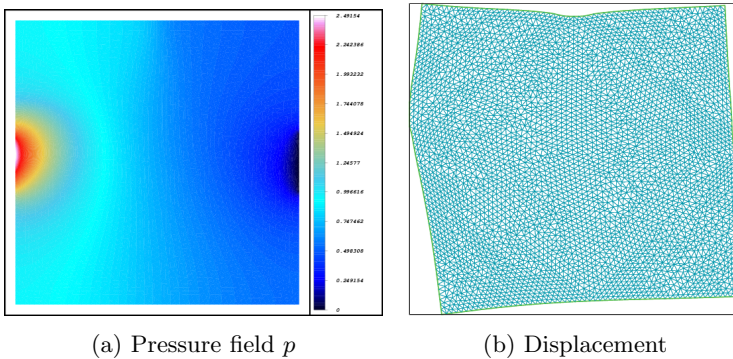


**Fig. 11** (a) State variable  $p$  (bar) and (b) the corresponding solid displacement (amplified  $\times 4$ ), for the two-physic problem of Section 6.1, in situation where  $\omega_1 = 2/5 \leq \omega_2 = 3/5$

The numerical values of the considered physical parameters are supplied by Fig. 9. Here, we consider two situations in (47): either  $\omega = 1 \geq \omega_2 = 0$  or  $\omega_1 = 2/5 \leq \omega_2 = 3/5$ . The functional  $J^*$  is minimized using the alternate directions algorithm of Section 5.1, subjected to a volume constraint  $\Theta = 44\%$  of the volume  $|\Omega|$ . On Fig. 10, the optimal density is displayed, while on Fig. 11, the corresponding pressure field and solid displacement are displayed. The optimal density  $\theta$  is represented in a gray scale: regions where  $\theta = 1$  are black (pure material), whereas white regions correspond to voids and, the gray regions correspond to the homogenized material with microstructures (periodically perforated by hexagonal cells); the topology of the solution is quite similar to that expected prior to the optimization. We note that, the algorithm tends to distribute more material in regions where the pressure gradient is high, of which we can clearly see a silhouette in the "shape" of a

beam, although contains a large composite zone at the center. However, in the situation where  $\omega_1 = 2/5 \leq \omega_2 = 3/5$ , the topology is more diffuse: it seems to be driven by the hydraulic power term.

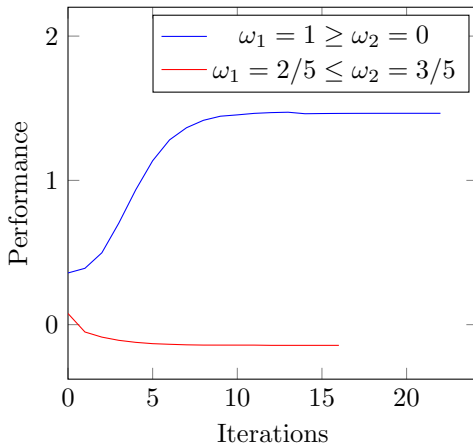


**Fig. 12** The convergence history for the two-physic topology optimization problem of Section 6.1, in both situations

For the pressure field  $p$ , we emphasize that the boundary conditions are respected: regions with high pressure gradient are located mainly on the beam and its becomes diffuse elsewhere. For this latter, the forcing induced by the fluid and the mechanical load are displayed by the displacement of solid  $u$ : see Fig. 11. On Fig. 12, we plot the convergence history for this calculation: smooth and relatively rapid convergence is observed.

## 6.2 A convective heat transfer problem

This second example is similar to that introduced and solved in [20], where the level-set method and a Stokes model for the fluid flow is employed. The computational domain is a square of dimension  $L$  (m), with two cavities, where a fluid of density  $\mathbf{q}_0$  ( $kgm^2s^{-1}$ ) and an inlet temperature  $T = T_{in}$  ( $^{\circ}C$ ) are flowing through the left-middle side boundary, while submitted to a pressure load  $p_0$  (bar) at the corresponding opposite side. In addition, a temperature  $T = T_1$  is prescribed on the lower and upper walls. All the other boundaries are insulated from the outside: zero Neumann boundary conditions hold for the temperature and pressure; see Fig. 13 for a schematic of this test case.

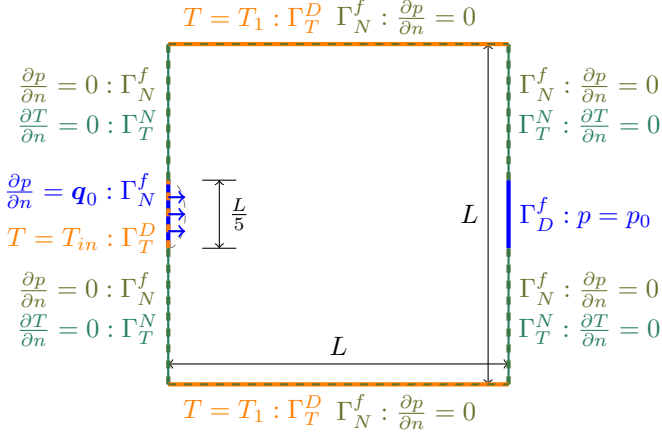


**Fig. 13** Setting of the convective heat transfer test case of Section 6.2.

For this example, we neglect the elastic contribution (namely, Eq. (28) is ignored), so that the example involves only a coupling of the flow (25) and heat equations (27). Our aim is to achieve a trade-off between the maximization of the hydraulic power dissipated by the fluid and the maximization of the heat transferred by the fluid, subjected to a volume constraint:

$$J^*(\theta, p(\theta), T(\theta)) = \omega \underbrace{\left( - \int_{\Omega} K^* \nabla p \cdot \nabla p \, dx \right)}_{\text{Hydraulic power}} + (1 - \omega) \left( \int_{\Omega} c_p K_D^* \nabla p \cdot \nabla T \, dx \right),$$

$$s.t. \left\{ \frac{1}{|\Omega|} \int_{\Omega} \theta \, dx = \Theta \right. \quad (48)$$

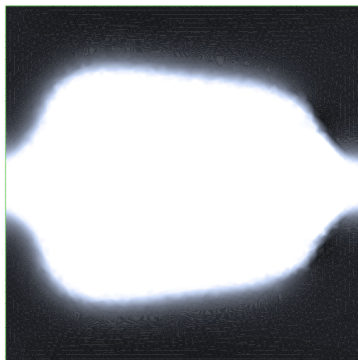
for some fixed coefficient  $\omega \in [0, 1]$  and a thermal capacity  $c_p$  ( $Jkg^{-1}K^{-1}$ ). We note that, the second term in (48) is seen as the opposite of heat transferred from the inlet  $\Gamma_N^f$  to the outlet  $\Gamma_D^f$  upon integration by parts:

$$\begin{aligned} \int_{\Omega} c_p K_D^* \nabla p \cdot \nabla T &= \int_{\Omega} -c_p \operatorname{div}(K^* \nabla p) T \, dx + \int_{\partial\Omega} c_p (K_D^* \nabla p \cdot n) T \, ds \\ &= \int_{\Gamma_N^f} c_p q_0 T \, ds + \int_{\Gamma_D^f} c_p \cdot 0 T_0 \, ds \end{aligned} \quad (49)$$

where the second term is a constant depending on the inlet data. The numerical values of the considered physical parameters are supplied by Fig. 14. Here, the fixed coefficient is set to  $\omega = 1/2$ , with volume constraint  $\Theta = 44\%$ .

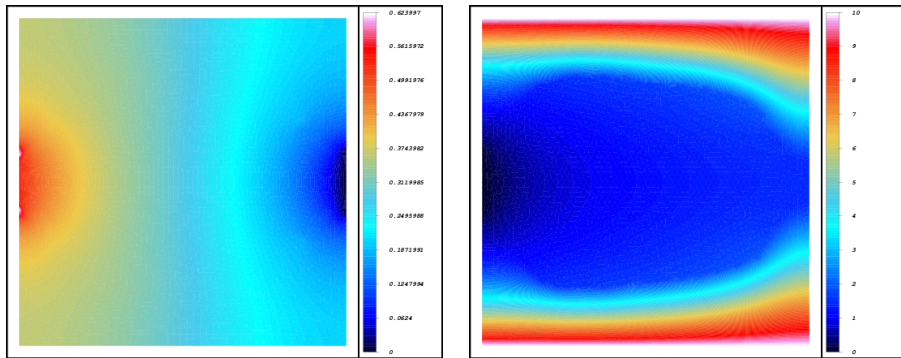
$L$	$q_0$	$p_0$	$T_{in}$	$T_1$	$c_p$	$k_s$	$k_f$
0.1	1	0	0	10	100	10	1

**Fig. 14** Numerical values of the physical parameters in the convective heat transfer problem of Section 6.2



(a) Density

**Fig. 15** The optimal density for the two-physic topology optimization problem of Section 6.2



(a) Pressure field  $p$

(b) Temperature  $T$

**Fig. 16** State variables  $p$  (bar),  $T$  ( $^{\circ}\text{C}$ ) for the optimized configuration of the two-physic problem of Section 6.2

The optimal density, and the corresponding state variables  $p$  and  $T$  are displayed by Fig. 15 and Fig. 16. The topology of the result is quite similar to that obtained in [20] (where the solution is autopenalized). We note that, the

algorithm tends to distribute more material in regions where the pressure gradient is low and temperature gradient is high, of which we can clearly see a silhouette in the "shape" of a pipe. For the pressure field  $p$ , we emphasize that the boundary conditions are respected: regions with high pressure gradient are located mainly at the center of the pipe and its becomes diffuse elsewhere. For the temperature field, we notice a cold down of the heat at the center of the pipe and its become hot elsewhere, with high temperature gradient: see Fig. 16. On Fig. 17, we plot the convergence history for this calculation: smooth and relatively rapid convergence is observed.

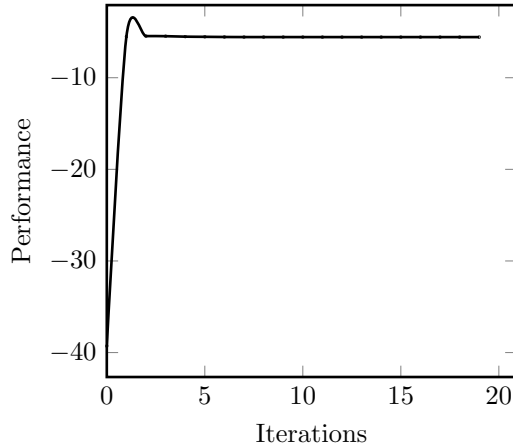


**Fig. 17** Convergence history for the two-physic topology optimization problem of Section 6.2

### 6.3 A thermal fluid-structure interaction problem

We finally turn to a topology optimization example in the full three-physic setting presented in Section 3; a test case which is new to the best of our knowledge. The computational domain is a square of dimension  $L$  (m), clamped on the middle-superior of the left-right side boundary  $\Gamma_D^s$  on a zone of width  $\frac{4}{50}L$ . In addition, a fluid of density  $\mathbf{q}_0$  ( $kgm^2s^{-1}$ ), and an inlet temperature  $T = T_{in}$  ( $^{\circ}C$ ) are flowing through the left-middle side boundary, while submitted to a pressure load  $p_0$  (bar) at the corresponding opposite side; a temperature  $T = T_1$  is prescribed on the lower and upper walls. All the other boundaries are insulated from the outside: zero Neumann boundary conditions hold for the temperature and pressure; see Fig. 18 for a schematic of this test case.

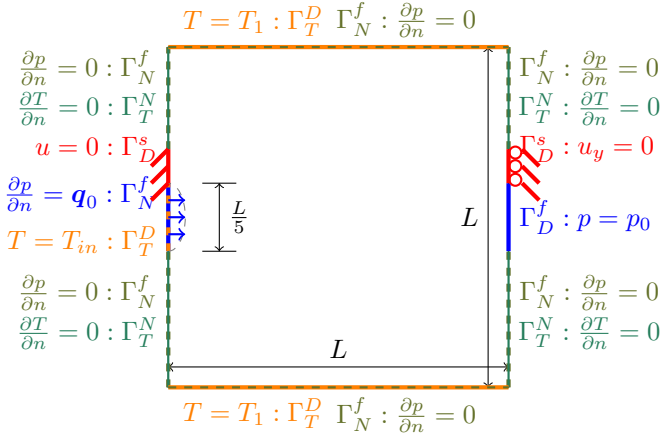


**Fig. 18** Setting of the three-physic problem of Section 6.3.

Our aim is to achieve a trade-off between minimization of the compliance of solid, the maximization of the hydraulic power dissipated by the fluid and the maximization of the heat transferred by the fluid, subjected to a volume constraint:

$$\begin{aligned}
 J^*(\theta, p(\theta), T(\theta), u(\theta)) = & \underbrace{\omega_1 \left( \int_{\Omega} A^* e(u) : e(u) \, dx \right)}_{\text{Elastic strain energy}} + \underbrace{\omega_2 \left( - \int_{\Omega} K^* \nabla p \cdot \nabla p \, dx \right)}_{\text{Hydraulic power}} \\
 & + \omega_3 \left( \int_{\Omega} c_p K_D^* \nabla p \cdot \nabla T \, dx \right), \\
 & \text{s.t. } \begin{cases} \frac{1}{|\Omega|} \int_{\Omega} \theta \, dx = \Theta \end{cases} \quad (50)
 \end{aligned}$$

for some fixed coefficients  $\omega_1, \omega_2, \omega_3 \in [0, 1]$ , such that  $\omega_1 + \omega_2 + \omega_3 = 1$ . The numerical values of the considered physical parameters are supplied by Fig. 19. Here, we consider two different fixed coefficients in (50): either  $\omega_1 = \omega_2 = \omega_3 = 1/3$  or  $\omega_1 = 1/5 < \omega_2 = \omega_3 = 2/5$ . For this latter, the volume constraint is set to  $\Theta = 23\%$ . The optimal density for each situation: either  $\omega_1 = \omega_2 = \omega_3 = 1/3$  or  $\omega_1 = 1/5 < \omega_2 = \omega_3 = 2/5$ , is displayed on Fig. 20. Very interestingly, we retrieve the fact that in situation where  $\omega_1 = \omega_2 = \omega_3 = 1/3$ , the topology of the solution contains a large composite zone at the center and a large contact surface with the fluid at entrance, namely, the left-middle side wall, so to reduce the effect of the pressure source; the algorithm tends to distribute more material in regions where the pressure gradient is high and it seems to be driven by the compliance (or elastic strain energy). In situation where  $\omega_1 = 1/5 < \omega_2 = \omega_3 = 2/5$ , the topology of the solution is homogeneous and it seems to achieve a trade-off between the minimization of the compliance



(of the solid) induced by the fluid, the maximization of the hydraulic power and of the heat transferred by the fluid.

$L$	$q_0$	$p_0$	$T_{in}$	$T_{ref}$	$T_1$	$\alpha$	$k_s$	$k_f$
0.1	1	0	0	0	10	1	10	1

**Fig. 19** Numerical values of the physical parameters in the three-physics problem of Section 6.3

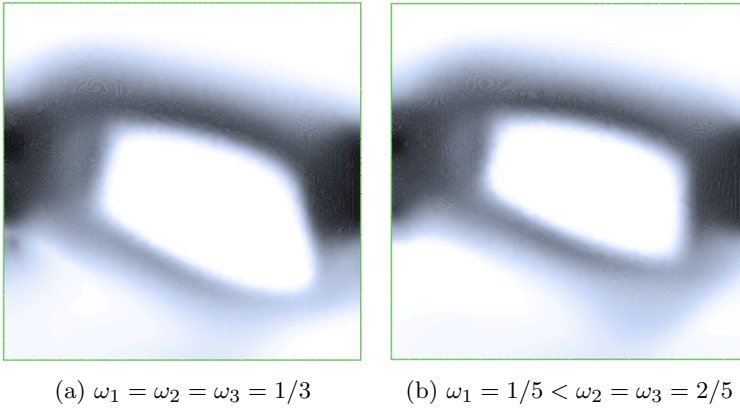


**Fig. 20** The optimal density for the three-physics problem of Section 6.3, in both situations

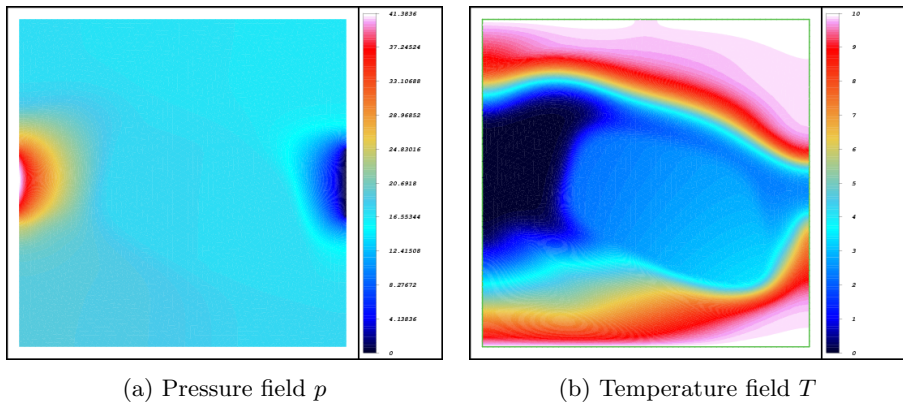


**Fig. 21** State variables  $p$  (bar) and  $T$  ( $^{\circ}C$ ) for the optimized configuration of the three-physics problem of Section 6.3, in situation where  $\omega_1 = \omega_2 = \omega_3 = 1/3$

In this example, the objective function  $J^*$  turns out to be very sensitive with respect to very small variations of the topology. The corresponding state variables  $p, T$  and deformed mesh are displayed by Fig. 21 and Fig 22, in situation where  $\omega_1 = \omega_2 = \omega_3 = 1/3$ . For this latter, we notice a cold down of the heat at the center of the optimal "shape" and its become hot elsewhere, with high pressure gradient located mainly at large solid regions: in both situations.

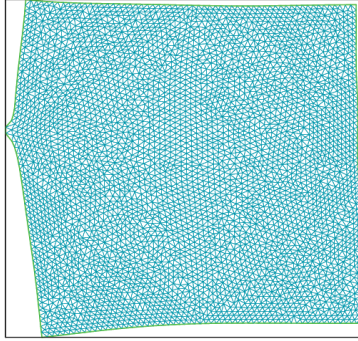


**Fig. 22** The solid displacement for the three-physic topology optimization problem of Section 6.3, in the situation  $\omega_1 = \omega_2 = \omega_3 = 1/3$

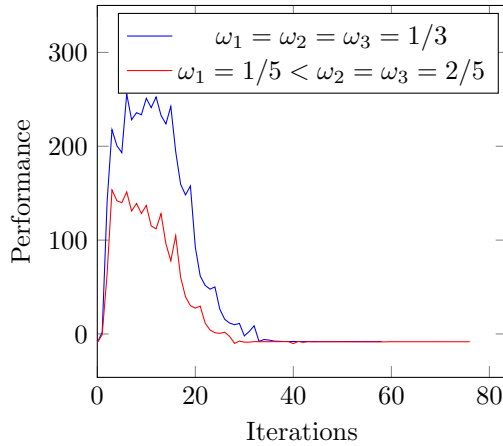


**Fig. 23** The convergence history for the three-physic topology optimization problem of Section 6.3, in both situations

The corresponding objective history in both situations: either  $\omega_1 = \omega_2 = \omega_3 = 1/3$  or  $\omega_1 = 0.2 < \omega_2 = \omega_3 = 0.4$ , is depicted on Fig. 23, while on Fig. 24, we plot the convergence history for the elastic strain energy, hydraulic power and

thermal strain energy, in the situation  $\omega_1 = \omega_2 = \omega_3 = 1/3$ . For this latter case, we note that in the first part of the optimization,  $J^*$  (as well as the elastic strain energy) increases sometimes substantially due to the fact that the volume constraint is not yet satisfied, or due to sudden discontinuities at topological changes. In addition, we can clearly see that in situation where  $\omega_1 = \omega_2 = \omega_3 = 1/3$ , the algorithm is driven by the compliance of the solid body as displayed by the topology of the result; see Fig. 20.

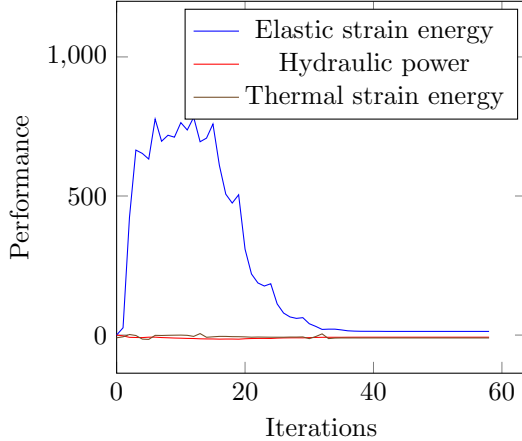


**Fig. 24** The convergence history for the elastic strain energy, the hydraulic power and thermal energy, in the situation  $\omega_1 = \omega_2 = \omega_3 = 1/3$

## 6.4 3-D thermal fluid interaction problem

This example is an attempt to compute a more realistic structure; it is the 3-D analog of the second example in Section 6.2. The computational domain is a 3-D cubic box of dimension  $L$  (m), with four cavities, where a fluid of density  $\rho_0$  ( $kgm^2s^{-1}$ ), and an inlet temperature  $T = T_{in}$  ( $^{\circ}C$ ) are flowing through the left-middle and back-middle surface of area  $\frac{1}{25}L$ , while submitted to a pressure load  $p_0$  (bar) at the corresponding opposite sides. In addition, a temperature  $T = T_1$  is prescribed on the lower and upper walls. All the other surfaces in this device are insulated from the outside: zero Neumann boundary conditions hold for the temperature and pressure; see Fig. 25 for a schematic of this test case.

We recall that for this example, the elastic model (28) is ignored; thus, it involves only a coupling of the flow (25) and heat equation (27). The objective is to achieve a trade-off between the maximization of the hydraulic power dissipated by the fluid and the maximization of the heat transferred by the fluid, subjected to a volume constraint; see (48) for the minimization problem.

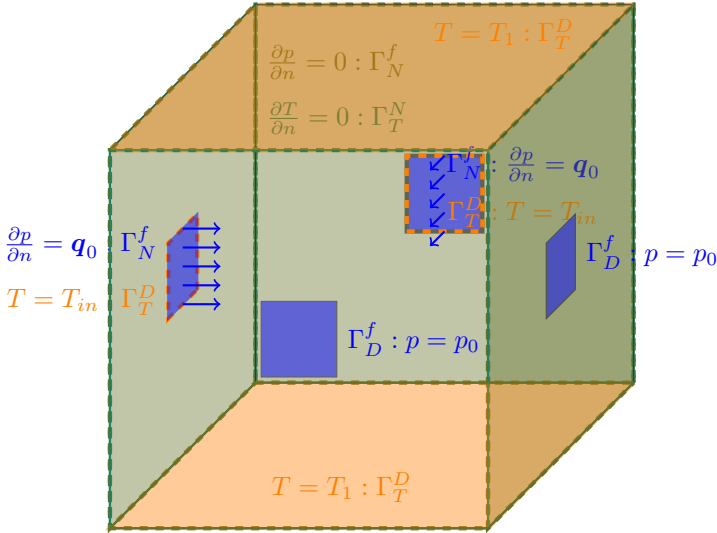


**Fig. 25** The setting of the 3-D two-physic problem of Section 6.4, subjected to fluid-thermal loads.

The functional  $J^*$  (48), is minimized using the alternate minimization algorithm of Section 5.1, under the constraint that the volume of the solid phase represent  $\Theta = 44\%$  of the total domain  $|\Omega|$ . The numerical values of the considered physical parameters are supplied by Fig. 14. We used for all finite element operations a mesh of size 119172 tetrahedral elements and started from an initial configuration  $\theta^0 = \Theta$ , throughout. The algorithm produces a symmetric layout. The total FreeFEM running CPU time (2.60 GHz) for this calculation is 5331 seconds.

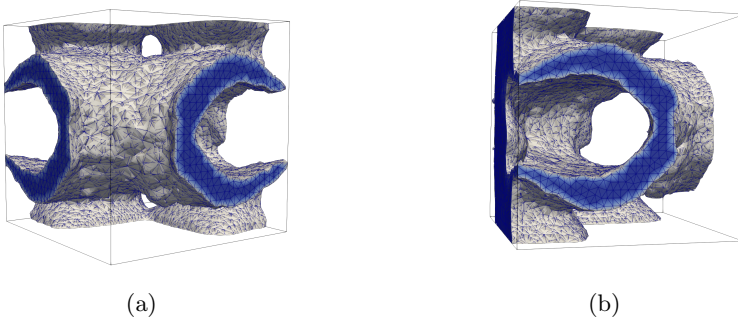


**Fig. 26** 3-D thermal fluid interaction problem of Section 6.4: composite solution, with respect to some fixed iso-surface  $\theta \geq 0.5$ .

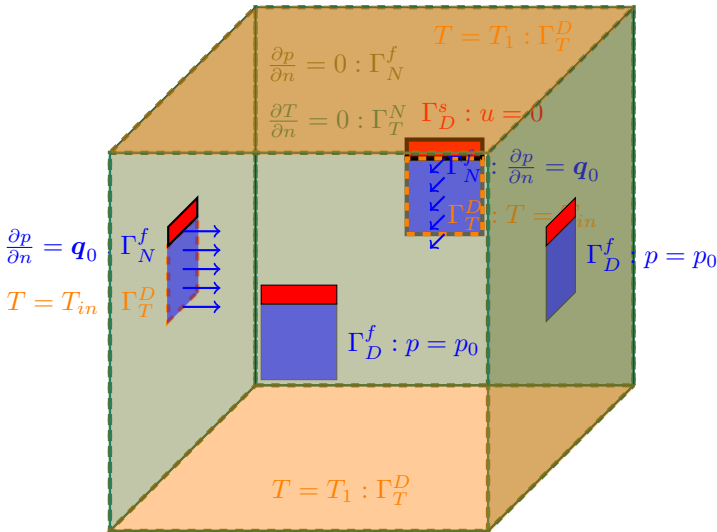
The 3-D pictures are harder to visualize. Fig. 26(a) represents the iso-surface  $\theta \geq 0.5$  of composite density. In this example, the iso-surfaces are smooth and

embedded into each other as  $\theta$  increases. The next picture Fig. 26(b), shows the design for some fixed rotation (counter-clock wise), the effect of which is to see another angle of the optimal composite "shape": the topology of solution is quite similar to that obtained in 2-D, namely, 3-D pipe-like "shape" is observed, although contains a large composite zone at its center.

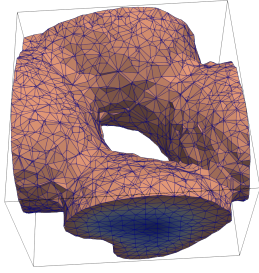
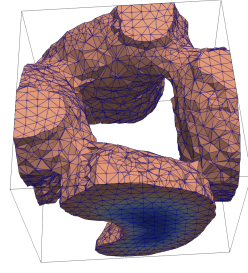
### 6.5 3-D thermal fluid-structure interaction problem

This final example is the 3-D analog of third example in Section 6.3. A cubic box is fixed on the middle-superior surface of its four cavities, where a fluid of density  $\mathbf{q}_0$  ( $kgm^2s^{-1}$ ) and an inlet temperature  $T = T_{in}$  ( $^{\circ}C$ ) are flowing through, while submitted to a pressure load  $p_0$  (bar) at the corresponding opposite sides. In addition, a temperature  $T = T_1$  is prescribed on the lower and upper walls; all the other surfaces in this device are insulated from the outside: zero Neumann boundary conditions hold for the temperature and pressure; see Fig. 27 for a schematic of this test case (see similar to the example in Section 6.4).

We recall that, the objective is to achieve a trade-off between the maximization of the hydraulic power dissipated by the fluid, the maximization of the heat transferred by the fluid and minimization of the compliance of the solid body, subjected to a volume constraint; see (50), for the optimization problem. Like the 2-D test case (6.3), we consider two different fixed coefficients in (50): either  $\omega_1 = \omega_2 = \omega_3 = 1/3$  or  $\omega_1 = 0.2 < \omega_2 = \omega_3 = 0.4$ ; the volume constraint is set to  $\Theta = 30\%$ . On Fig. 28, we displayed the iso-surface  $\theta \geq 0.3$  of composite density for each situation: either  $\omega_1 = 1 \geq \omega_2 = \omega_3 = 0$  or  $\omega_1 = \omega_2 = \omega_3 = 1/3$ ; and on Fig. 29, the corresponding solid displacement is displayed.



**Fig. 27** The setting of the 3-D three-physic problem of Section 6.5, subjected to fluid-thermal loads. On the red rectangles, the solid are clamped.

(a)  $\omega_1 = 1 \geq \omega_2 = \omega_3 = 0$ (b)  $\omega_1 = \omega_2 = \omega_3 = 1/3$ 

**Fig. 28** 3-D three-physic problem of Section 6.5: composite solution, with respect to some fixed iso-surface  $\theta \geq 0.3$ , in both situations.

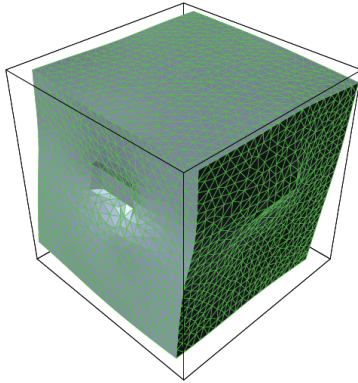


**Fig. 29** The solid displacement for the three-physic topology optimization problem of Section 6.5, in the situation  $\omega_1 = \omega_2 = \omega_3 = 1/3$

Very interestingly, we retrieve the fact that the topology of the result is quite similar to that obtained in the 2-D case, for both configurations: either  $\omega_1 = 1 \geq \omega_2 = \omega_3 = 0$  or  $\omega_1 = \omega_2 = \omega_3 = 1/3$ ; however, in situation where  $\omega_1 = 1 \geq \omega_2 = \omega_3 = 0$ , the topology of the solution contains a large composite zone at the center and a large contact surface with the fluid at entrance, so to reduce the effect of the pressure source; which is to be expected because the objective (in situation where  $\omega_1 = 1 \geq \omega_2 = \omega_3 = 0$ ) is to minimize the compliance of solid body. In situation where  $\omega_1 = \omega_2 = \omega_3 = 1/3$ , the topology of the solution is homogeneous and it seems to achieve a trade-off between the minimization of the compliance (of the solid) induced by the fluid, the maximization of the hydraulic power and of the heat transferred by the fluid.

Hence, we emphasize that in 3-D, the topology of the solution is better than in 2-D, where a large contact surface with the fluid at entrance was observed, so to reduce the effect of the pressure source; see Fig. 20.

## 7 Conclusions

In this study, we have demonstrated the relevance of shape and topology optimization for generating unconventional design problems involving two or three-physic interactions using the homogenization method. In our proposed method, Biot-Darcy's law and the convection-diffusion equation are employed to characterize the pressure (of the fluid flow) and the temperature (of the heat flux); the effect of which is to weakly couple to the solid phase by solving the associated PDEs using the standard finite element method. The porosity of each finite element is related to the material density through a smooth enough function to ensure a smooth transition between void and solid phase; the physical parameters (for fluid and heat flow) are numerically computed in the case of isotropic porous medium. The method facilitates calculation of the load sensitivities with respect to the design variables, using the adjoint-state method; it is noticed that consideration of load sensitivities within the approach does alter the composite designs and, are particularly important when designing multi-physic systems. In contrast to methods that use explicit boundary tracking, the Biot-Darcy's model, together with our simplified heat transfer equation offer the potential for relatively straightforward extension to 3-D problems. The effectiveness and robustness of the proposed homogenization method is verified by minimizing several arbitrary objective functionals.

**Acknowledgments.** This research project was fully sponsored by IFPEN: IFP énergies nouvelles; and was supported by Pierre Viot: design and simulation engineer at IFPEN.

## Declarations

On behalf of all authors, the corresponding author states that there is no conflict of interest.

## Replication of results

On behalf of all authors, the corresponding author states that there is no codes available as supplementary material because this work is carried out as part of a thesis in partnership with IFPEN. The latter holds the intellectual rights.

## References

- [1] Allaire, G., Shape Optimization by the Homogenization Method, Springer, Applied Mathematical Sciences, 146 (2002).
- [2] Murat, F., Contre-exemples pour divers problèmes où le contrôle intervient dans les coefficients, *Ann. Mat. Pura Appl.*, 112 (1997) 49-68.
- [3] Kohn, R.V. and Strang, G., Optimal design and relaxation of variational problems, I. *Comm. Pure Appl. Math.*, 39(1) (1986) 113-137.
- [4] Lurie, K.A. and Cherkaev, A.V. and Fedorov, A.V., Regularization of optimal design problems for bars and plates, I, II. *J. Optim. Theory Appl.*, 37(4) (1982) 499-522, 523-543.
- [5] Bendsøe, M.P. and Kikuchi, N., Generating optimal topologies in structural design using a homogenization method, *Comput. Methods Appl. Mech. Engrg.*, 71(2) (1988) 197-224.
- [6] Bendsøe, M.P., Optimal shape design as a material distribution problem, *Structural and multidisciplinary optimization*, 1(4) (1989) 193-202.
- [7] Bendsøe, M.P. and Sigmund, O., *Topology optimization: theory, methods, and applications*, Springer Science & Business Media, (2003).
- [8] Allaire, G. and Geoffroy-Donders, P. and Pantz, O., Topology optimization of modulated and oriented periodic microstructures by the homogenization method, *Computers & Mathematics with Applications*, 78(7), (2019) 2197-2229.
- [9] Allaire, G., *Conception optimale de structures*, Springer Berlin, Heidelberg, (2007).



- [10] Céa, J., Conception optimale ou identification de formes, calcul rapide de la dérivée directionnelle de la fonction coût, *ESAIM: Mathematical Modelling and Numerical Analysis*, 30(6) (1986) 371-402.
- [11] Hammer, V.B. and Olhoff, N., Topology optimization of continuum structures subjected to pressure loading, *J. Structural and Multidisciplinary Optimization*, 19(2) (2000) 85-92.
- [12] Du, J. and Olhoff, N., Topological optimization of continuum structures with design-dependent surface loading - Part I: New computational approach for 2D problems, *J. Structural and Multidisciplinary Optimization* 27(3) (2004) 151-165.
- [13] Fuchs, M.B. and Shemesh, NNY., Density-based topological design of structures subjected to water pressure using a parametric loading surface, *J. Structural and Multidisciplinary Optimization*, 28(1) (2004) 11-19.
- [14] Zheng, B. and Chang, C.J. and Gea, H.C., Topology optimization with design-dependent pressure loading, *J. Structural and Multidisciplinary Optimization*, 38(6) (2009) 535-543.
- [15] Lee, E. and Martins, JRRA., Structural topology optimization with design-dependent pressure loads., *J. Computer Methods in Applied Mechanics and Engineering*, 40-48 (2012) 233-236.
- [16] Li, Zm and Yu, J. and Yu, Y. and Xu, L., Topology optimization of pressure structures based on regional contour tracking technology, *J. Structural and Multidisciplinary Optimization*, 58(2) (2018) 687-700.
- [17] Mendes, E. and Sivapuram, R. and Rodriguez, R. and Sampaio, M. and Picelli, R., Topology optimization for stability problems of submerged structures using the TOBS method, *Computers & Structures*, 259 (2022) 106-685.
- [18] Wang, C. and Zhao, M. and Ge, T., Structural topology optimization with design-dependent pressure loads, *Structural and Multidisciplinary Optimization*, 53(5):1005-1018 (2016).
- [19] Picelli, R. and Neofytou, A. and Kim, HA., Topology optimization for design-dependent hydrostatic pressure loading via the level-set method, *Structural and Multidisciplinary Optimization*, 60(4):1313-1326 (2019).
- [20] Feppon, F. and Allaire, G. and Bordeu, F. and Cortial, J. and Dapogny, C., Shape Optimization of a Coupled Thermal Fluid-Structure Problem in a Level Set Mesh Evolution Framework, *J. Boletín de la Sociedad Española de Matemática Aplicada*, Springer 76(3) (2019) 413-458.

- [21] Kumar, P. and Frouws, J.S. and Langelaar, M., Topology Optimization of Fluidic Pressure Loaded Structures and Compliant Mechanisms using the Darcy Method, Springer: Structural and Multidisciplinary Optimization, 61 (2020) 1637-1655.
- [22] Kumar, P., TOPress: a MATLAB implementation for topology optimization of structures subjected to design-dependent pressure loads, Springer: Structural and Multidisciplinary Optimization 66, 97 (2023).
- [23] Hübner, D. and Rohan, E. and Lukeš, V. and Stingl, M., Optimization of the porous material described by the Biot model, Elsevier, International Journal of Solids and Structures, 156-157 (2019) 216-233.
- [24] Murat, F.. and Simon, J., Sur le contrôle par un domaine géométrique, rapport la 189, univ, Paris VI, (1976).
- [25] Henrot, A. and Pierre, M., Variation et optimisation de formes: une analyse géométrique, Springer Science & Business Media, (2006).
- [26] Murat, F. and Tartar, L., Calcul des variations et homogénéisation, Les lectures de l'homogénéisation : théorie et applications en physique, (Eyrolles, 1985) 319-369.
- [27] Pantz, O. and Trabelsi, K., A post-treatment of the homogenization method for shape optimization, SIAM Journal on Control and Optimization, 47(3) (2008) 1380-1398.
- [28] Geoffroy-Donders, P., Homogenization method for topology optimization of structures built with lattice materials, PhD thesis, Université Paris Saclay (COMUE), 2018.
- [29] Neuber, H., Theory of notch stresses: principles for exact calculation of strength with reference to structural form and material, USAEC Office of Technical Information, (1961) 4547.
- [30] Abad, K.M.E. and Khanoki, A.S. and Pasini, D.F., Fatigue design of lattice materials via computational mechanics: Application to lattices with smooth transitions in cell geometry, International Journal of Fatigue, 47 (2013) 126-136.
- [31] Vigdergauz, S., Energy-minimizing inclusions in a planar elastic structure with macroisotropy, Structural optimization, 17(2-3) (2013) 104-112.
- [32] Lin, C.Y. and Kikuchi, N. and Hollister, J., A novel method for biomaterial scaffold internal architecture design to match bone elastic properties with desired porosity, Journal of biomechanics, 43(5) (2004) 623-636.

- [33] Hashin, Z. and Shtrikman, S., A variational approach to the theory of the elastic behaviour of multiphase materials, *Journal of the Mechanics and Physics of Solids*, 11(2) (1963) 127-140.
- [34] Batchelor, G., *An introduction to fluid dynamics*, Cambridge university press, 2000.
- [35] Jobic, Y. and Kumar, P. and Topin, F. and Occelli, R., Transport properties of solid foams having circular strut cross section using pore scale numerical simulations, *Heat Mass Transfer*, 54 (2018) 2351–2370.
- [36] Allaire, G. and Kohn, R.V., Optimal design for minimum weight and compliance in plane stress using extremal microstructures, *Europ. J. Mech. A/Solids*, 12(6) (1993) 839-878.
- [37] Suzuki, K. and Kikuchi, N., A homogenization method for shape and topology optimization, *Comp. Meth. Appl. Mech. Eng.*, 93 (1991) 291-318.
- [38] Hecht, F., *J. Math. Anal. Appl.*, New development in freefem++, *J. Numerical Mathematics*, (2012).